

**MASARYKOVA
UNIVERZITA**

**PŘÍRODOVĚDECKÁ FAKULTA
ÚSTAV TEORETICKÉ FYZIKY A ASTROFYZIKY**

Bakalářská práce

BRNO 2025

NINA DUCHYŇOVÁ

MASARYKOVA UNIVERZITA
PŘÍRODOVĚDECKÁ FAKULTA
ÚSTAV TEORETICKÉ FYZIKY A ASTROFYZIKY

M U N I Department
S C I of Theoretical Physics
and Astrophysics

Why do not all radio galaxies form extended structures?

Bakalářská práce

Nina Duchyňová

Vedoucí práce: Anna Patrycja Wójtowicz, Ph.D.
Brno 2025

Bibliografický záznam

Autor:	Nina Duchyňová Přírodovědecká fakulta, Masarykova univerzita Ústav teoretické fyziky a astrofyziky
Název práce:	Proč všechny rádiové galaxie nevytvářejí rozšířené struktury?
Studijní program:	Fyzika
Studijní obor:	Astrofyzika
Vedoucí práce:	Anna Patrycja Wójtowicz, PhD.
Akademický rok:	2024/2025
Počet stran:	xvi+ 63
Klíčová slova:	Aktivní galaktická jádra; Jety; Kompaktní rádiové zdroje; Rozšířené rádiové zdroje; Vlastnosti hostitelské galaxie; DLM diagram; BPT diagram; Green Valley diagram; KS test; ROGUE; IRAS

Bibliographic Entry

Author: Nina Duchyňová
Faculty of Science, Masaryk University
Department of Theoretical Physics and
Astrophysics

Title of Thesis: Why do not all radio galaxies form extended
structures?

Degree Programme: Physics

Field of Study: Astrophysics

Supervisor: Anna Patrycja Wójtowicz, PhD.

Academic Year: 2024/2025

Number of Pages: xvi+ 63

Keywords: Active galactic nuclei; Jets; Compact radio sources;
Extended radio sources; Host galaxy properties;
DLM diagram; BPT diagram; Green Valley dia-
gram; KS test; ROGUE; IRAS

Abstrakt

V této závěrečné práci zkoumáme rozdíly mezi kompaktními a rozšířenými rádiovými zdroji prostřednictvím analýzy jejich fyzikálních vlastností a vlastností hostitelských galaxií. Naše analýza vychází z katalogu ROGUE (Radio sources associated with Optical Galaxies and having Unresolved or Extended morphologies, tj. rádiové zdroje přiřazené k optickým galaxiím s nerozlišenou nebo rozšířenou morfologií). Nejprve identifikujeme rádiové zdroje pomocí klasifikačních diagramů, jako jsou DLM a BPT diagramy, abychom určili, zda jsou galaxie klasifikovány jako aktivní galaktická jádra (AGN), hvězdotvorné galaxie, nebo zda se jejich klasifikace mezi jednotlivými diagramy liší. Následně analyzujeme dalekoinfračervenou svítivost a rádiovou svítivost při frekvenci 1,4 GHz, abychom posoudili, zda emise pochází převážně z oblastí tvorby hvězd, nebo zda naznačuje nadbytek rádiového záření. Pro hlubší pochopení povahy těchto zdrojů porovnáváme různé vlastnosti hostitelských galaxií, včetně lineárního rozměru, optické morfologie, hvězdné hmotnosti, Balmerova dekrementu, prachového ztemnění, míry tvorby hvězd, bolometrické a Eddingtonovy svítivosti a hmotnosti černé díry. V závěru využíváme tzv. Green Valley diagram k prozkoumání možnosti, že kompaktní zdroje mohou vytvářet malé výtrysky (jety) v důsledku slapových jevů (tidal disruption events).

Abstract

In this thesis, we investigate the differences between compact and extended radio sources by analysing their physical properties as well as the host galaxy properties. Our analysis is based on the ROGUE catalogue (Radio sources associated with Optical Galaxies and having Unresolved or Extended morphologies). We begin by identifying radio sources using diagnostic classification diagrams, such as the DLM and BPT plots, to determine whether the galaxies are classified as AGN, star-forming, or exhibit differing classifications across the two plots. We then analyse the far-infrared luminosity and the 1.4 GHz radio luminosity to assess whether the emission originates primarily from star formation or indicates a radio excess. To further explore the nature of these sources, we compare various host galaxy properties, including linear size, optical morphology, stellar mass, Balmer decrement, dust attenuation, star formation rate, bolometric and Eddington luminosities, and black hole mass. Finally, we employ the Green Valley diagram to explore the possibility that compact sources may produce small jets as a result of tidal disruption events.

BACHELOR'S
THESIS DESCRIPTION

Academic year: 2024/2025

Department:	Department of Theoretical Physics and Astrophysics
Student:	Nina Duchyňová
Programme:	Physics
Specialization:	Astrophysics

In compliance with the Study and Examination Regulations of Masaryk University, the Department Head of *ústavu* at the Faculty of Science, MU is assigning you a Bachelor's thesis with the title:

Title of the thesis/dissertation:	Prečo všetky rádiové galaxie nevytvárajú rozšírené štruktúry?
Title of the thesis in English:	Why do not all radio galaxies form extended structures?
Language used:	English

Final Description:

Študent bude pracovať s údajmi z katalógu ROGUE, najväčšej databázy rádiových galaxií s identifikovanými optickými hosťami, ktoré majú SDSS spektrá. Z tohto katalógu si študent vyberie vzorku kompaktných rádiových zdrojov a porovnávaciu vzorku rozšírených rádiových galaxií. Na zodpovedanie otázky, prečo niektoré rádiové galaxie nevyvíjajú rozšírené rádiové štruktúry, študent analyzuje rôzne parametre hosťielskych galaxií, ako sú rýchlosť tvorby hviezd, rýchlosť akrecie, hviezdna hmotnosť a ďalšie, a vykoná štatistické testy na identifikáciu najvýznamnejších rozdielov medzi oboma vzorkami.

The student will work with data from the ROGUE catalog, the largest database of radio galaxies with identified optical hosts that have SDSS spectra. From this catalog, the student will select a sample of compact radio sources and a comparison sample of extended radio galaxies.

To address the question of why some radio galaxies do not develop extended radio structures, the student will analyze various host parameters, such as star formation rate, accretion rate, stellar mass, and others, and perform statistical tests to identify the most significant differences between the two samples.

Thesis supervisor:	Anna Patrycja Wójtowicz, PhD.
Thesis assignment date:	2024/11/12
In Brno, date:	2025/03/19

The description was approved through IS MU.

Nina Duchyňová, 2024/11/18

Anna Patrycja Wójtowicz, PhD., 2024/11/19

RNDr. Luboš Poláček, 2024/12/04

Poděkování

My deepest gratitude goes to Dr. Anna Patrycja Wójtowicz, for her guidance, for her willingness to always find time for me and for answering the ultimate question of them all: "Why do our plots look like that?" Without her encouragement, writing this thesis would have been far more challenging. Thank you.

To my parents and family, who supported me every step of the way, even when they didn't fully understand what it is that I do. Their love and encouragement made it possible for me to get this far and study astrophysics. I could not have done this without you. Thank you.

To my friends I made on this journey. During the three years we have spent in building number six, we have built not just a great community but lifelong friendships. You have shown me that studying physics can even be fun when you are surrounded by the right people. Thank you.

Finally, I would like to express my admiration to all the physicists, astrophysicists, astronomers, and scientists who came before us, building the path for the knowledge we have today. Thank you.

Prohlášení

Prohlašuji, že jsem svoji bakalářskou práci vypracovala samostatně pod vedením vedoucího práce s využitím informačních zdrojů, které jsou v práci citovány.

Brno

.....
Nina Duchyňová

Contents

Introduction	1
1 From Nebulae to Galaxies	3
1.1 Optical morphology	4
1.1.1 Elliptical Galaxies	4
1.1.2 Spiral Galaxies	5
1.1.3 Lenticular Galaxies	5
1.1.4 Distorted Galaxies	5
2 The Universe of Active Galaxies	7
2.1 The Shining Cores - AGN	7
2.2 Radio galaxies	8
2.3 Extended radio sources - FR classification	9
2.4 Compact radio sources	10
3 Understanding Host Galaxies	11
3.1 Galaxy mass	11
3.2 Star formation (rate)	11
3.3 Black hole mass	12
3.4 Accretion	13
4 Visualizing and Validating	17
4.1 Bolometric and Eddington luminosity	17
4.2 Radio Luminosity at 1.4 GHz	18
4.3 Far-Infrared Luminosity	18
4.4 DLM diagram	19
4.5 FIR and radio correlation	20
4.6 Balmer decrement	21
4.7 H α Equivalent Width	21
4.8 BPT diagram	21
4.9 Green Valley diagram	23
5 Statistical methods - 1D and 2D KS tests	25
5.1 1D KS test	25
5.2 2D KS test	25
6 The Roots of Data	27
6.1 ROGUE I/II	27

6.2	STARLIGHT	28
6.3	IRAS	29
7	Sample selection	31
7.1	BPT diagram	32
7.2	DLM diagram	33
7.3	FIR and total radio luminosity	34
8	Analysing the data	39
8.1	Linear size	39
8.2	Host galaxy properties	41
8.2.1	Redshift distribution	41
8.2.2	Optical morphology	41
8.2.3	Stellar Mass	43
8.2.4	Dust attenuation and Balmer decrement	44
8.2.5	Starformation rate	45
8.3	AGN properties	47
8.3.1	Eddington and bolometric luminosity	47
8.4	Green Valley diagram	51
9	Summary	55

Introduction

The universe — a vast, peculiar, and captivating place — home to countless galaxies. Among them, radio galaxies stand out, with not only extremely luminous cores but with outflows and jets created by a colossal central engine known as a supermassive black hole.

Yet, not all radio galaxies are the same. Some launch jets that extend far beyond their visible boundary, while others remain compact with confined engines. This difference sparks a lot of questions. Why do not all radio galaxies form extended structures? Could it be due to the environment of the host galaxy? Maybe the nature of the central black hole has an influence. Or is there an underlying mechanism yet to be understood?

In this thesis, we seek to find at least a small part of the answer to these questions. By examining the host galaxy properties and star formation and employing diagnostic tools, we aim to shed some light on this problem.

1 From Nebulae to Galaxies

Our story begins in 1909, at the Lick Observatory, where Edward Fath decided to unravel the nature of so-called "spiral nebulae". These were considered relatively nearby, gaseous objects, similar to the Orion nebula, or perhaps collections of unresolved stars. His goal was to determine whether these nebulae exhibited a continuous spectrum, like a cluster of stars, or a bright line spectrum, known to be a characteristic of gaseous nebulae. While most spiral nebulae displayed continuous spectra, the NGC 1068 revealed both bright and continuous spectra, with one of those lines previously identified in the spectra of gaseous nebulae. In the following years, many other astronomers observed this phenomenon, including Edwin Hubble.

Between 1912 and 1917, Vesto Slipher measured the redshifts of spiral nebulae, revealing that they were moving too quickly to be part of the Milky Way. This finding sparked the beginning of the well-known great debate between Harlow Shapley and Heber Curtis, while Shapley thought that all of the spiral nebulae were in the Milky Way, hinting that there is only one galaxy with everything in it, Curtis was convinced by the measured redshift, suggesting that they were further away making them separate galaxies.

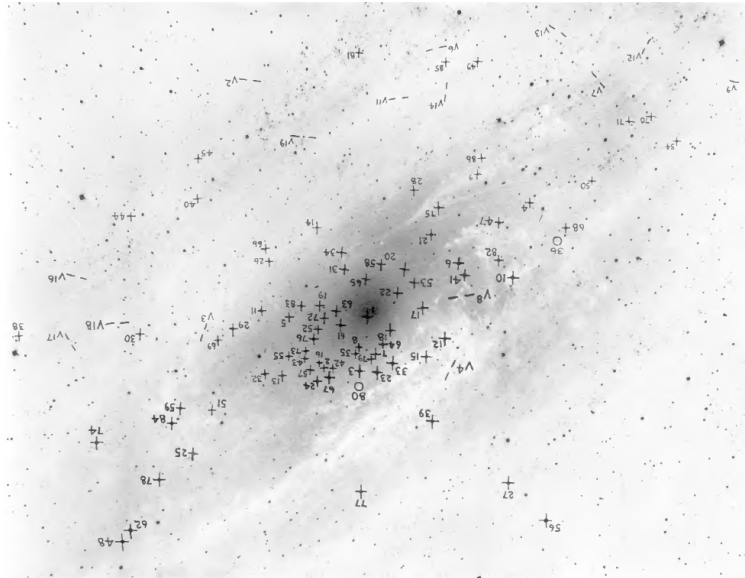


Figure 1: Plate taken by Duncan using Hooker Telescope at Mount Wilson, with markings of novae and variables by Hubble. Credit: [Hubble \(1929\)](#)

The debate was finally resolved in 1925, when Edwin Hubble published a groundbreaking paper on Cepheid variable stars he had discovered in Messier 31 ([Hubble, 1929](#)), also known as the Andromeda Galaxy. Using the 100-inch Hooker Telescope at Mount Wilson, Hubble identified these stars and, by applying their period-luminosity relation, he was able to determine that the

distance to M31 exceeded even Shapley's proposed extent of the Milky Way. This discovery conclusively showed that M31 was, in fact, a separate galaxy, just like ours.

1.1 Optical morphology

The term "nebulae" for galaxies continued to be used even in Edwin Hubble's renowned work *The Realm of the Nebulae* (Hubble, 1936). In this influential paper, Hubble tried to bring order to the chaotic universe of galaxies by attempting to classify them. This led to the development of the Hubble Sequence, a classification framework that remains fundamental even to galaxy studies today.

To visualise this classification, Hubble introduced the "tuning fork" diagram, which divides galaxies into "early-type" galaxies on the left and "late-type" galaxies on the right.

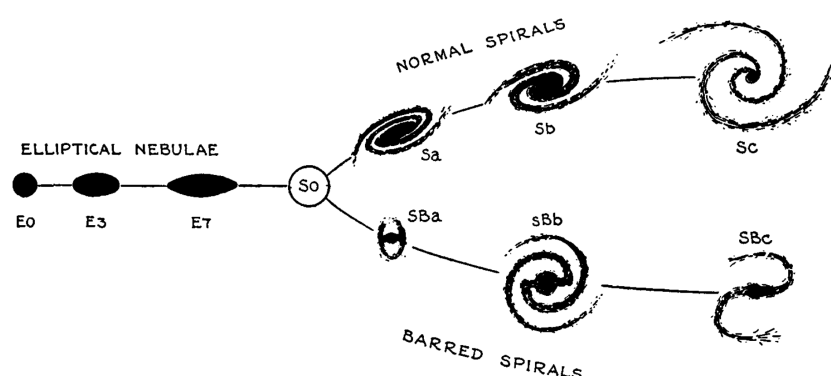


Figure 2: Hubble's "tuning-fork" as depicted in *The Realm of the Nebulae* (Hubble, 1936)

Initially, this division suggested a possible evolutionary pathway for galaxies, with elliptical galaxies on the left evolving into spiral galaxies over time. However, modern research has shown that this is not necessarily the case. The terms "early-type" and "late-type" remain popular and continue to help astronomers categorise galaxies based on their characteristics Longair (2008).

The primary optical divisions used in this thesis are elliptical, spiral, lenticular, and distorted galaxies - a widely used classification which began with Hubble's *The Realm of the Nebulae*.

1.1.1 Elliptical Galaxies

Elliptical galaxies lack well-defined structural features, typically exhibiting a spheroidal or elliptical shape. These galaxies are often the most luminous and, due to their lack of gas and dust for new star formation, elliptical galaxies

contain mostly old stars. They can be classified based on their shape. The range is from nearly circular (E0) to highly elongated (E7).

1.1.2 Spiral Galaxies

Spiral galaxies are distinguished by their prominent spiral arms, which form a disc-like structure. The arms extend from a central bulge, which may be elliptical or elongated. This bulge is the focal point of the galaxy's structure, from which the spiral arms emerge. These galaxies contain both old and new stars, with new stars forming mainly in the arms. Spiral galaxies are further classified into Sa, Sb and Sc based on how tightly wound their arms are.

1.1.3 Lenticular Galaxies

Lenticular galaxies share features with both elliptical and spiral galaxies. Like spirals, they possess a central bulge, which can be either "ordinary" or "barred." They also have a disk but lack the distinct spiral arms typical of spiral galaxies. Lenticular galaxies are commonly found in dense galaxy clusters, where environmental effects might strip away their gas, stopping the star formation.

1.1.4 Distorted Galaxies

Distorted galaxies are difficult to classify due to their irregular, non-symmetrical shapes. These galaxies do not exhibit a dominant nucleus or a clear structure, making them stand out as chaotic.



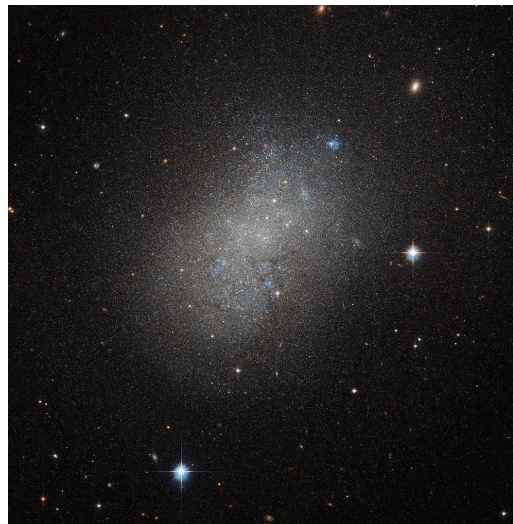
Elliptical galaxy



Spiral galaxy



Lenticular galaxy



Distorted galaxy

Figure 3: Optical morphology types. Credit: [NASA \(2024\)](#)

2 The Universe of Active Galaxies

At the Owens Valley Radio Observatory in 1960, Sandage photographed a stellar object with a faint nebulosity. While the object appeared star-like, its photometric data revealed that the object was variable with an excess of ultraviolet emission, which is not common for classical stars. Over time, more star-like objects showing similar characteristics were discovered. Astronomers soon realised that many of these objects also emitted radio waves and displayed broad emission lines. These objects came to be known as quasi-stellar sources (QSO), or quasars. It wasn't long before scientists realised that something unusual might lie at the core of these objects, a discovery that later evolved into the concept of active galactic nuclei.

2.1 The Shining Cores - AGN

Active galaxies are one of the most energetic phenomena in the universe, emitting significantly more energy at shorter wavelengths than their non-active counterparts, where the radiation is mostly coming from stars and interstellar gas. The intense electromagnetic radiation of an active galaxy originates in a highly energetic core known as an active galactic nucleus (AGN), a compact region in the centre of the galaxy.

Active galaxies are generally categorised into two main types: Seyfert galaxies and quasars. The key distinction between them lies in their luminosity. In Seyfert galaxies, the nucleus emits an amount of visible light comparable to the combined output of all the galaxies' stars. This makes the nucleus and the host galaxy easily distinguishable. In contrast, quasars are significantly more luminous, radiating at least 100 times the total stellar energy of their host galaxies, which makes the host galaxy harder to detect more clearly.

Alternatively, based on optical spectroscopy, AGN can be categorised into broad and narrow emission-line regions. Broad emission lines are produced by fast-moving gas located close to the black hole, within the so-called broad-line region (BLR). In contrast, narrow emission lines originate from slower-moving gas that resides farther from the nucleus in the narrow-line region (NLR). This central region is surrounded by dust and gas, called a torus, that absorbs radiation and is therefore crucial for galaxy characteristics.

The AGN unification model suggests that all AGN have the same central engine and structure, with observed differences primarily due to the orientation of the torus relative to our line of sight. If we observe the torus from the side, we can only see the NLR, leading to the observation of Seyfert 2 galaxies. If we are able to look at its centre, where BLR is located, we can identify Seyfert 1 galaxies.

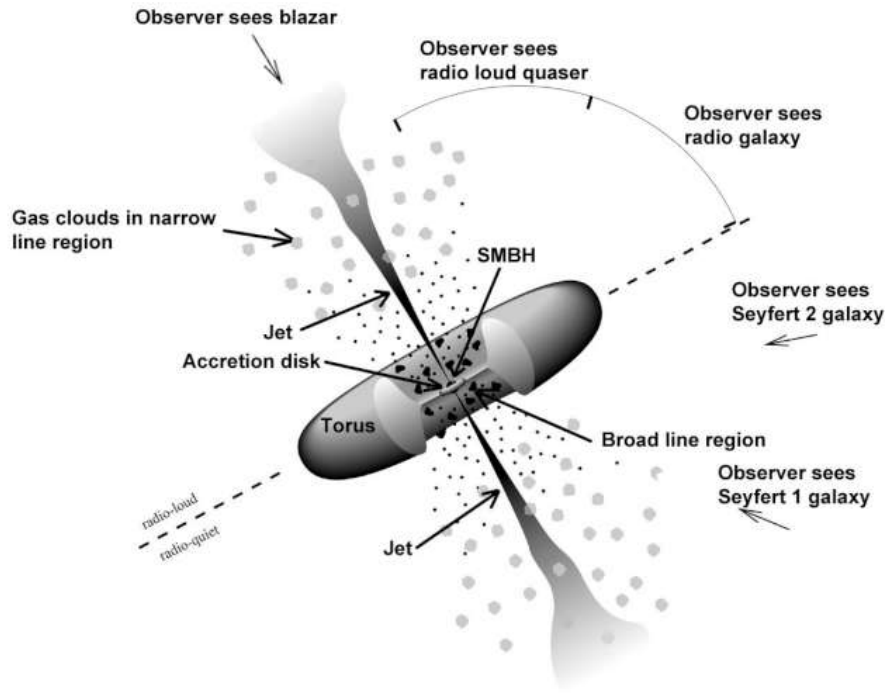


Figure 4: AGN unification model. Credit: [NASA Fermi Science Team \(2025\)](#)

2.2 Radio galaxies

It was already in 1932 when Jansky concluded that there is radio radiation coming from the disk of the Milky Way, with the strongest signals coming right from the Galactic centre. This discovery was not intentional. Jansky had initially been investigating sources of static that interfered with transatlantic radio communications. However, his findings unexpectedly opened a new door for astronomers, marking the beginning of radio astronomy.

Currently, researchers divide radio galaxies into radio-loud (RL) and radio-quiet (RQ). Radio-loud galaxies are usually large elliptical galaxies, distinguished by their intense emission in the radio band. Their luminosities are typically on the order of $L_{\text{radio}} \geq 10^8 L_{\odot}$ or $\geq 3 \times 10^{41} \text{ erg s}^{-1}$ ([Rosswog and Brüggem, 2007](#)). The source of this strong radio emission can be traced to the active nucleus of the galaxy or the lobes, which can extend several kiloparsecs from the nucleus. These lobes are often connected to the nucleus by relativistic jets, powerful, collimated beams of charged particles ejected from the nucleus in opposite directions, which can extend across vast distances, ranging from a few light-years to thousands or even millions of light-years. In some cases, when the jet is pointed directly toward us, we observe a blazar. An object that is both exceptionally luminous and highly variable. RQ galaxies, on the other hand, emit radio emissions at 1.4 GHz up to $< 10^{30.3} \text{ erg s}^{-1} \text{ Hz}^{-1}$.

The radio emission from RL sources is primarily produced through a process known as synchrotron emission, where high-energy charged particles,

such as electrons, spiral around magnetic fields at relativistic speeds, emitting non-thermal radiation. This mechanism is responsible for the signature radio emission seen in many active galaxies, especially in those with jets and lobes.

In star-forming galaxies (SFG), free-free emission (thermal bremsstrahlung) might contribute to the spectrum. Free-free emission arises in the ionised HII regions, where free electrons scatter off ions without being captured, resulting in the release of low-energy photons. However, the contribution from free-free emission is negligible for galaxies with dominant AGN.

There is also thermal emission, which is predominantly in the infrared spectrum, which originates in hot dust and ionised gases. These are heated by the radiation from the AGN.

But what powers the radio core of these galaxies? The energy that fuels the radio core typically originates from the rotational energy of the supermassive black hole at the galaxy's centre or the gravitational energy released as matter falls onto the black hole's accretion disk.

2.3 Extended radio sources - FR classification

It was 1974 when Bernard Lewis Fanaroff and Julia Margaret Riley published a paper on extended radio galaxies, where they classified them into two distinct categories, known as FR I and FR II (Fanaroff and Riley, 1974).

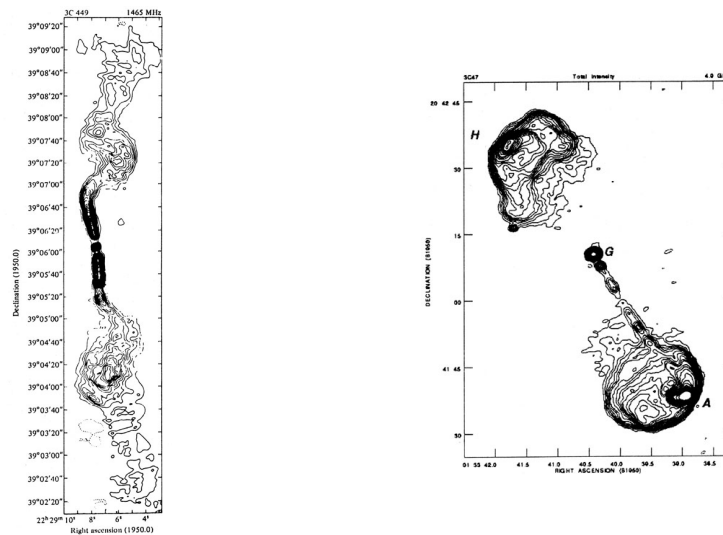


Figure 5: VLA maps of Fanaroff-Riley classification. The picture on the left is FR I and the right is FR II. Credit: Database (2025)

The primary distinction between these two classes lies in the distribution of their radio emission. FR I galaxies have their brightest radio emission concentrated near the galaxy's centre, gradually fading toward the edges of

the lobes, while FR II galaxies are distinguished by their powerful jets, which extend outward and terminate in bright hot spots at the lobes' edges. This results in a concentration of radio emission in the outermost regions, making them more luminous than their central areas.

The brightness distribution is closely related to the power of the jets and their interaction with the surrounding gas and dust. In FRI galaxies, the jets are less powerful than those in FR II galaxies, causing them to slow down as they reach the outer regions of the galaxy. As a result, the jets remain concentrated near the AGN, where particles interact with the material in the core of the galaxy. In contrast, the jets in FR II galaxies are far more powerful, stretching out to the outer regions where they collide with the intergalactic medium, creating structures known as hotspots.

2.4 Compact radio sources

Nowadays, we also identify compact radio sources (CRS), a class of AGN that are unresolved at small angular sizes. These sizes are typically less than a few arcseconds, which means they appear as a single point or a tiny object in radio images (Baldi, 2023).

While Fanaroff and Riley (1974) focused solely on extended sources, the classification of FR 0 galaxies has since been found. These are a type of weak RL CRSs, typically found in galaxies known as Core Galaxies. Core Galaxies have a bolometric luminosity from their radio core and AGN comparable to weak FRI galaxies, but their extended radio emission is a lot weaker (Baldi, 2023).

Powerful CRSs like peaked sources (PS) and compact steep spectrum (CSS) sources are usually large, bright elliptical galaxies. The stellar population is mostly older, with some star formation occurring in the galaxy (O'Dea and Saikia, 2021). It is thought that the PS and CSS source make up a big part of FR 0.

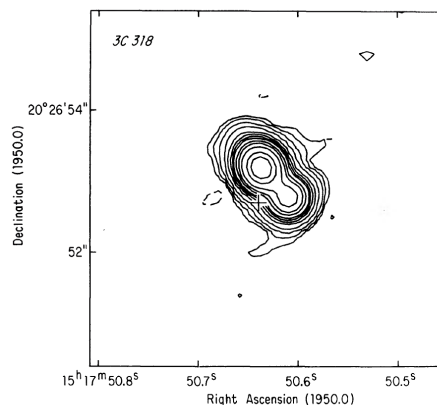


Figure 6: VLA map of a compact radio galaxy. Credit: Pearson et al. (1985)

3 Understanding Host Galaxies

The properties of the host galaxy play a crucial role in understanding the nature of its active nucleus, providing valuable information on the relationship between the central AGN and its environment. In this chapter, we are going to focus on some of the features of the AGN and their host galaxies.

3.1 Galaxy mass

The total mass of a galaxy includes all baryonic and dark matter. The mass can be divided into the total stellar mass (M_*), interstellar medium (gas and dust), dark matter, and the central supermassive black hole (M_{BH}).

The stellar mass is usually calculated by measuring the luminosity of the galaxy and estimating the right mass-to-light ratio (M_*/L). This ratio is not constant but depends on different factors such as the age of the stars, their metallicity, and the initial mass function, to name a few.

The ROGUE catalogue (more in [subsection 6.1](#)) includes calculated data using the STARLIGHT code, which uses the spectral synthesis. The stellar mass can be estimated by decomposing a galaxy's observed spectrum into a combination of simple stellar populations of various ages and properties. Individual simple stellar populations have known mass-to-light fractions, and after fitting the light fractions, STARLIGHT can estimate the total stellar mass of the galaxy.

3.2 Star formation (rate)

Star formation rate (SFR) describes the rate at which a galaxy forms new stars. It is typically measured in solar masses per year. In [Bouwens et al. \(2011\)](#), the authors presented a graph of galaxies at various redshifts ([Figure 7](#)). Their analysis suggests that the SFR increased in the early universe, reaching a peak around redshift 2.5, after which it gradually declined.

As we discussed earlier, star formation is closely linked to a galaxy's mass, so to quantify this relation better, researchers introduced the concept of the specific star formation rate (sSFR). The sSFR measures how efficiently a galaxy forms stars relative to its total stellar mass (M_*):

$$\text{sSFR} = \frac{\text{SFR}}{M_*}. \quad (1)$$

A high sSFR indicates that a galaxy is actively forming stars, whereas a low sSFR suggests reduced star formation activity. In some cases, a galaxy may enter a quenching phase, where star formation gradually stops.

Several factors contribute to quenching, as discussed in [Sánchez Almeida et al. \(2014\)](#). One possible reason is that when a galaxy grows too massive, incoming gas from the cosmic web heats up as it enters the halo, making star

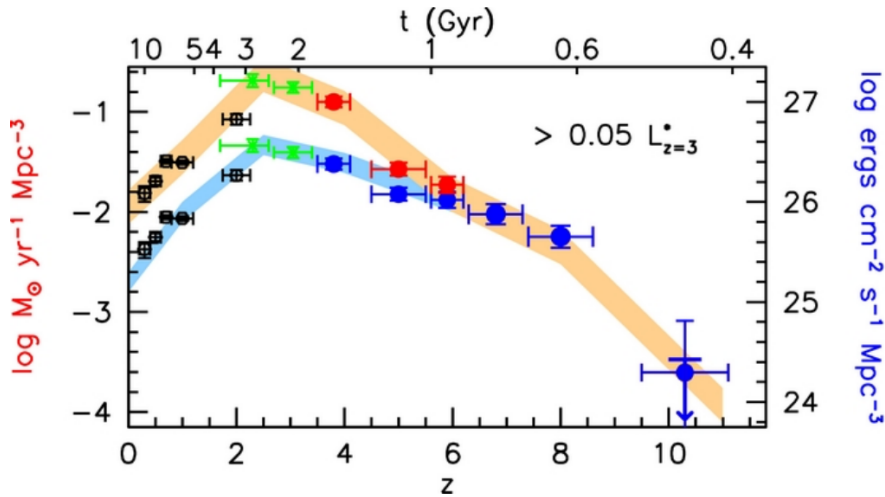


Figure 7: SFR as a function of redshift (z), where blue points and blue region refer to the observations before dust correction, while red points and orange regions are observations after dust correction. Credit: [Bouwens et al. \(2011\)](#)

formation hard or even stopping it. Another quenching mechanism is a rapid initial burst of star formation, which quickly uses the available gas needed to sustain future star formation. Additionally, AGN feedback plays a role as an active galactic nucleus can release energy, pushing gas away from the galactic centre and making it less available for new stars to form. Of course, more reasons can result in the quenching of star formation, these are just a few we mentioned.

3.3 Black hole mass

Another important characteristic of the host galaxy is the black hole mass (M_{BH}). The properties of a host galaxy and the central black hole are suggested to be closely linked together, indicating that the black hole's activity and host galaxy can influence each other ([Heckman and Best \(2014\)](#) and [Kormendy and Ho \(2013\)](#)).

The black hole mass can be estimated using the "direct" or "indirect" methods. The direct methods utilise dynamical models that rely on spatially resolved kinematic tracers, such as stars or dust orbiting around the black hole. In addition, reverberation mapping can also be used. A method that measures time delays between light variations and gas response to determine the size of the broad-line region. Another direct approach is the megamaser technique, which measures black hole mass by tracking water masers orbiting in a disk and using their velocities and positions to apply Kepler's laws.

The direct estimates are challenging, and BH masses can be obtained directly only for a few hundred of the closest objects. We thus need to rely on indirect methods, motivated observationally. The most commonly used

approach utilises the correlation between stellar velocity dispersion (σ) and the BH mass (REFS), pointing toward BH–host galaxy co-evolution (Ferrarese and Merritt (2000) and Gebhardt et al. (2000)).

Other indirect methods use the galaxy’s luminosity (L) or effective radius (R). It has been shown that the relation between black hole mass, luminosity, and radius ($M_{\text{BH}} \propto (L/R)^{3.8}$) yields nearly identical results to the $M_{\text{BH}}\text{--}\sigma$ relation. Black hole mass can also be estimated using the galaxy’s size and stellar mass ($M_{\text{BH}} \propto (M_{\star}/R)^{2.9}$). Nonetheless, the correlation between black hole mass and velocity dispersion exhibits minimal scatter and applies even to galaxies without a predominant bulge, making it the most universal method (van den Bosch, 2016).

The black hole mass estimated for sources in ROGUE (more in subsection 6.1), were obtained using the correlation between the black hole mass (M_{BH}) and the stellar velocity dispersion (σ), in the form given in Tremaine et al. (2002). This method utilises the Doppler effect, noting that the wavelengths from stars moving away from us experience redshift, while the ones moving towards us are shifted towards blue. The shifts broaden the absorption lines, which reflect the range of stellar velocities in each part of the galaxy, which can help us estimate the black hole mass even in elliptical galaxies that do not rotate systematically. This relation was expressed as:

$$\log \frac{M_{\text{BH}}}{[M_{\odot}]} = 8.13 + 4.16 \cdot \log \frac{\sigma}{[200 \text{ km s}^{-1}]} \quad (2)$$

Where the stellar velocity dispersion (σ) is measured in effective radius, and was calculated for our sources through the spectral analysis using the STARLIGHT code by averaging the fitted broadening of the absorption lines.

3.4 Accretion

To understand the energy produced by a supermassive black hole, we can draw an analogy to an object falling toward Earth (Rosswog and Brügggen, 2007). Let’s consider an object in free fall toward Earth, such as a meteorite. As it descends, potential energy converts into kinetic energy, ultimately transforming into heat upon impact. A similar process occurs in the gas surrounding a supermassive black hole: the black hole’s gravity pulls the gas inward, increasing its velocity until it falls in, releasing radiation.

The mass accretion rate ($\dot{m} = \frac{\Delta M}{\Delta t}$) tells us how much matter is accreted by a compact object in a certain amount of time. This quantity cannot be measured directly, which is why astronomers need to rely on other observable parameters like bolometric and Eddington luminosities. These can also give us some insight into the structure of the disk, which is possible because we can relate the bolometric luminosity (L_{bol}) to the mass accretion rate (\dot{m}) as:

$$L_{\text{bol}} = c^2 \eta_{\text{bol}} \dot{M}, \quad (3)$$

where c is the speed of light in the vacuum and η_{bol} is the radiative efficiency of converting the energy to bolometric luminosity, varying with the accretion rate.

We introduce the Eddington limit, which is a parameter describing the maximal possible rate at which the matter can fall onto the compact object. Whenever the accretion approaches the Eddington limit, the matter falling into the black hole starts to be blown away by the radiation pressure. For the accretion approaching the Eddington limit, the radiative efficiency is $\eta_{\text{Edd}} = 0.1$. More about bolometric and Eddington luminosities in [subsection 4.1](#).

Considering the above-mentioned, one can get some insight into the mass accretion rate (\dot{m}) by looking at the so-called Eddington ratio (λ), and this way study the structure of the disk. The Eddington ratio is given as a ratio of bolometric to Eddington luminosity:

$$\lambda \sim \frac{L_{\text{bol}}}{L_{\text{Edd}}}. \quad (4)$$

Generally, we can consider two types of accretion disks. The first one is called Shakura-Sunyaev ([Shakura and Sunyaev, 1973](#)). This type of disk is characteristic of higher accretion rates with Eddington ratio $\lambda > 0.01$. Shakura-Sunyaev disk emits the disk's energy most efficiently in the UV and optical waveband, which leads to efficient cooling of the accretion flow. The solution is a geometrically thin but optically thick disk.

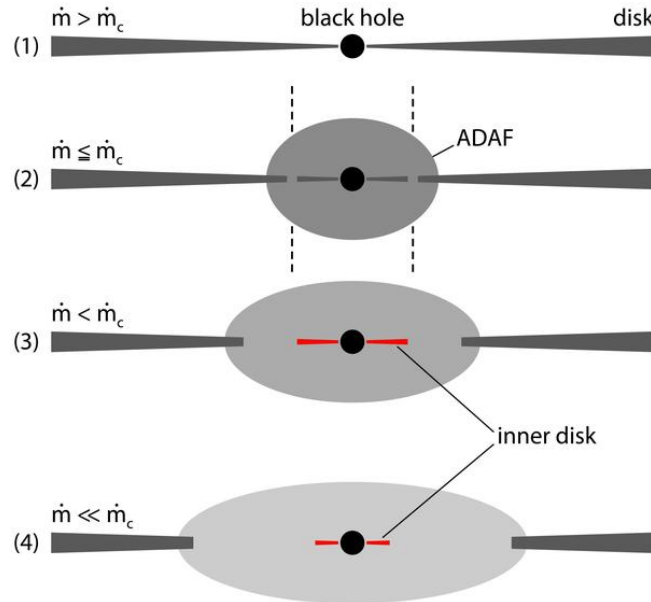


Figure 8: Transition from thin Shakura-Sunyaev to thick ADAF accretion disk. The \dot{m}_c is the critical rate, where the transition between the two happens, and \dot{m} is the mass accretion rate. Credit: [Meyer-Hofmeister, E. and Meyer, F. \(2011\)](#)

The second type of disk occurs whenever the mass accretion rate is low, and the bolometric luminosity is much smaller than the Eddington luminosity ($\lambda \ll 0.01$). The disk becomes geometrically thick but optically thin, as the radiation cannot efficiently escape the accretion flow. The solution is described as the ADAF (advection-dominated accretion flow) model (Narayan and Yi, 1995). ADAF emits most of its energy in broadband; however, as the accretion flow cannot efficiently cool the gas down, it becomes very hot, making it easier to be detected in X-rays.

The transition between these two types is not abrupt, but is rather smooth as the two solutions can coexist together (Yuan and Narayan, 2014) (see Figure 8), particularly when $\lambda \lesssim 0.01$.

4 Visualizing and Validating

In this chapter, we are going to focus on the key diagnostic methods and parameters used to characterise radio-emitting AGN and distinguish these sources from radio galaxies with emission dominated by star formation activity.

4.1 Bolometric and Eddington luminosity

The bolometric luminosity (L_{bol}) tells us how much energy a galaxy creates at all wavelengths and can be estimated using various scaling relations, obtained by comparing measurable quantities. In our case, we utilise two methods to estimate the bolometric luminosity: the $\text{H}\alpha$ emission line, which is created by hydrogen atoms excited by the UV radiation of the accretion disk and the [OIII] emission line. The bolometric luminosity from the $\text{H}\alpha$ line is then calculated using an equation given in [Sikora et al. \(2013\)](#):

$$L_{\text{bol}} = 2 \cdot 10^3 L_{\text{H}\alpha}. \quad (5)$$

In [Sikora et al. \(2013\)](#), they stated that the bolometric luminosity calculated via $\text{H}\alpha$ line is better, since the bolometric luminosity calculated via [OIII] line ($L_{[\text{OIII}]}$) is controlled by the ionisation state of the gas. However, [Stasińska et al. \(2025\)](#) found a very good correlation between $L_{[\text{OIII}]}$ and L_{bol} , contrary to this belief, given by the equation:

$$\log L_{\text{bol}} = (0.7715 \pm 0.0023) \log L_{[\text{OIII}]} + (4.3839 \pm 0.0145). \quad (6)$$

The Eddington luminosity (L_{Edd}) represents the upper limit of luminosity that an accretion-powered source can sustain over time. If the luminosity exceeds this limit, the radiation pressure overcomes the gravitational force, causing the gas to be expelled. To calculate the Eddington limit, we can use the equation from [Rosswog and Brügger \(2007\)](#):

$$L_{\text{Edd}} = \frac{4\pi GM_{\text{BH}}m_{\text{p}}c}{\sigma_{\text{T}}} \sim 3 \cdot 10^{13} \left(\frac{M_{\text{BH}}}{10^9 M_{\odot}} \right) L_{\odot} \sim 1.3 \cdot 10^{31} M_{\text{BH}}, \quad (7)$$

where m_{p} is the mass of the proton, M_{BH} is the mass of the black hole, c is the speed of the light and σ_{T} is the Thomson cross section. This can be considered the maximum possible luminosity of a mass-powered source undergoing spherical accretion. For this calculation, three assumptions were made. Firstly, we assume pure, ionised hydrogen for the Thomson cross-section. Secondly, spherical symmetry and lastly, a stationary state.

4.2 Radio Luminosity at 1.4 GHz

The synchrotron radio emission occurs whenever a charged relativistic particle in the magnetic field is accelerated. These conditions are found both in star-forming regions as well as in the vicinity of the AGN.

The radio emission at 1.4 GHz in SFR is primarily due to synchrotron radiation from relativistic electrons accelerated by supernova remnants, created by a more massive stellar population. This results in a strong relation between the 1.4 GHz luminosity and SFR as established by [Murphy et al. \(2011\)](#) and given by the equation:

$$\left(\frac{\text{SFR}_{1.4, \text{GHz}}}{M_{\odot} \text{yr}^{-1}} \right) = 6.35 \cdot 10^{-29} \cdot \left(\frac{L_{1.4, \text{SFR}}}{\text{erg s}^{-1} \text{Hz}^{-1}} \right), \quad (8)$$

Yet, the equation was created under the assumption that the emission at 1.4 GHz is primarily from star formation, with little to no AGN contribution.

However, radio luminosity can also arise from an AGN, where jets or lobes produce strong radio emissions. In many cases, this AGN-driven emission far exceeds that of star formation, resulting in an overestimation of SFR. To determine the dominant source of radio emission in a galaxy, scientists use the concept of radio excess. A high radio excess indicates the presence of additional non-thermal emission, most likely originating from the mentioned AGN. We can calculate the radio excess as [Equation 9](#), where we subtract the luminosity associated with the star formation ($L_{1.4, \text{SFR}}$) from the total luminosity of the galaxy ($L_{1.4, \text{total}}$).

$$\text{radio excess} = L_{1.4, \text{total}} - L_{1.4, \text{SFR}} \quad (9)$$

4.3 Far-Infrared Luminosity

A different way to study the star formation and stellar population is by Far-infrared luminosity (L_{FIR}), created when young, massive stars produce UV and optical radiation, which is then absorbed and re-emitted by interstellar dust. Far-infrared luminosity can be calculated as:

$$L_{\text{FIR}} = F_{\text{FIR}} \cdot 4 \pi d^2. \quad (10)$$

Broad-band FIR flux (F_{FIR}) can be obtained by using the equation [Equation 11](#) from [Helou et al. \(1988\)](#), which utilises the narrow band flux density at 60 μm ($f_{\nu}(60 \mu\text{m})$) and 100 μm ($f_{\nu}(100 \mu\text{m})$).

$$F_{\text{FIR}} = 1.26 \cdot 10^{-14} \cdot (2.58 \cdot f_{\nu}(60 \mu\text{m}) + f_{\nu}(100 \mu\text{m})). \quad (11)$$

4.4 DLM diagram

The DLM diagram was first introduced by [Best et al. \(2005\)](#). Its name comes from the three key parameters utilised in the graph: $D_n(4000)$, $L_{1.4, \text{total}}$, and M_* . The $D_n(4000)$ index is the measured strength of a break at 4000 Å in the spectrum of a galaxy, which is primarily caused by metal absorption lines in the atmospheres of older stars. The strength of this break increases in galaxies with a higher fraction of old, metal-rich stars, making it a useful indicator of stellar population age. This information can further help us to classify whether a galaxy is SF or AGN.

The combination of $D_n(4000)$ and $L_{1.4}/M_*$ is particularly good for distinguishing SFGs from AGN, since SFGs lack (or have minimal) additional radio emission from an AGN, they tend to show lower $L_{1.4}/M_*$ values, and given that they actively form new stars, the $D_n(4000)$ parameter tends to be lower as well, showing the SFGs in the lower left corner of the diagram. AGN would show higher values and thus concentrate in the upper right corner.

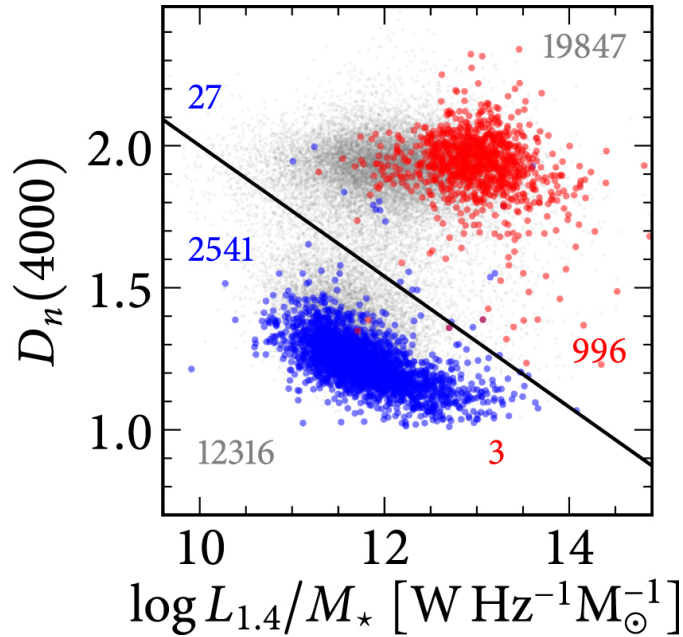


Figure 9: DLM diagram with blue points being star-forming galaxies based on the BPT diagram, while red points are FR I and FR II radio sources. Credit: [Kozieł-Wierzbowska et al. \(2021\)](#)

In [Kozieł-Wierzbowska et al. \(2021\)](#), the DLM diagram was applied to ROGUE I galaxies, leading to the identification of a new dividing line between AGN and SFGs ([Figure 9](#)), expressed as [Equation 12](#), and since we also work with the ROGUE catalogue (more about ROGUE in [subsection 6.1](#)), we decided to use this line for our graph as well.

$$D_n(4000) = -0.23 \cdot L_{1.4}/M_* + 4.3 \quad (12)$$

4.5 FIR and radio correlation

As mentioned earlier, FIR occurs when young stars heat the dust, while radio luminosity is created by accelerating electrons by supernova remnants, meaning both of these methods can give us an insight into the star population and star formation rate in the galaxy. However, if a galaxy hosts an AGN, the radio emission may be significantly influenced by AGN activity, potentially complicating the interpretation of the FIR-radio correlation. While a few weak AGN could follow the FIR vs. radio correlation, the majority tend to diverge from the anticipated relationship. Hence, the FIR vs. radio luminosity can help us identify if the dominant source of radio emission is star-forming regions or AGN outflows. This relation was first identified by [van der Kruit \(1971\)](#), but they did not explicitly take into account the radio from AGN.

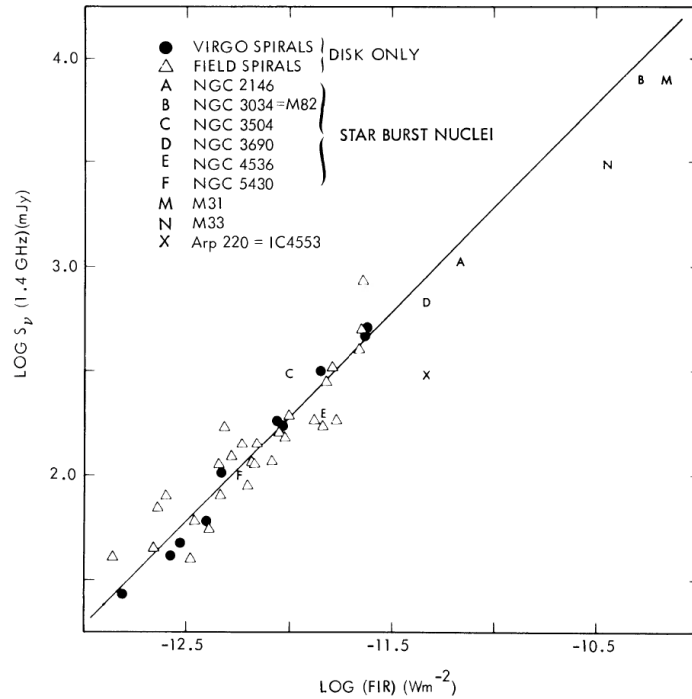


Figure 10: FIR vs. radio luminosity at 1.4 GHz for galaxies with extended emission and no compact radio component. Credit: [Helou et al. \(1985\)](#)

The FIR vs. radio relation is linear, but there is no fundamental theoretical equation. Instead, it is expressed in terms of the logarithmic ratio between the far-infrared and radio luminosities, first introduced in [Helou et al. \(1985\)](#), called the q factor ([Equation 13](#)), where $L_{1.4, \text{total}}$ is the total radio luminosity at 1.4 GHz and F_{FIR} is far-infrared flux.

$$q = \log \left(\frac{F_{\text{FIR}}/3.75 \cdot 10^{12} \text{W m}^{-2}}{L_{1.4, \text{total}}/\text{W m}^{-2} \text{Hz}^{-1}} \right). \quad (13)$$

Yun et al. (2001) estimate that for star-forming galaxy (SFGs) the q factor is around 2.34 ± 0.10 , meaning that FIR emission is about 200 times stronger than radio emission. Galaxies dominated by the AGN would have lower values since the radio emission is enhanced by jets. Del Moro et al. (2013) calculated the q factor for RL AGN to be -0.38 , while for galaxies with a "normal" amount of radio emission, $q = 2.21 \pm 0.18$.

4.6 Balmer decrement

The Balmer series is a set of spectral lines in hydrogen, produced when electrons transition from higher energy levels to the second energy level of the hydrogen atom. The $H\alpha$ and $H\beta$ lines are the most noticeable in the optical spectrum and are frequently detected in regions where hydrogen gas is illuminated by a strong source of radiation.

In astrophysics, it is well established that the $H\alpha$ and $H\beta$ emission lines originate in the same regions within a galaxy. However, because they have different wavelengths, they interact with dust in different ways, which affects the way we observe the lines on Earth. By comparing the observed wavelengths and intensities of these lines to their expected values from laboratory measurements, we can estimate the amount of dust present in the galaxy.

This method is commonly used to determine the Balmer decrement ($A_{V,\text{Balmer}}$), which serves as a proxy for dust extinction within the host galaxy.

4.7 $H\alpha$ Equivalent Width

The equivalent width (EW) of the $H\alpha$ emission line (6563 \AA) measures the line's strength in comparison to the underlying stellar continuum. $H\alpha$ emission is produced by photoionisation, driven either by star formation, AGN or both. In Cid Fernandes et al. (2011), researchers aimed to define a boundary distinguishing whether the emission is mainly from hot low-mass evolved stars (HOLMES) or from the AGN. They determined that $H\alpha = 3 \text{ \AA}$ serves as a suitable threshold. They suggest that for galaxies with $H\alpha$ below 3 \AA , AGN might still be present, but compared to hot low-mass evolved stars, the ionisation coming from an AGN is weak. At 3 \AA , the estimated AGN contribution to the ionisation is between $\frac{1}{3}$ and $\frac{2}{3}$, while below 1 \AA the AGN is negligible.

4.8 BPT diagram

In 1981, Baldwin, Phillips, and Terlevich published a seminal paper (Baldwin et al., 1981), using intensity ratios of emission lines to distinguish emission-line galaxies from QSOs based on their primary excitation mechanism.

The graph they introduced, now known as the BPT diagram, utilises the ratios $[\text{OIII}]/H\beta$ vs. $[\text{NII}]/H\alpha$. This diagram is widely used to differentiate galaxies with normal star formation from those hosting AGN. Over time,

numerous researchers have tried to refine the boundary that best separates AGN from SFGs using ionisation models and observational data. Two of the most widely adopted functions for this classification were proposed by [Kauffmann et al. \(2003\)](#) and [Kewley et al. \(2001\)](#)

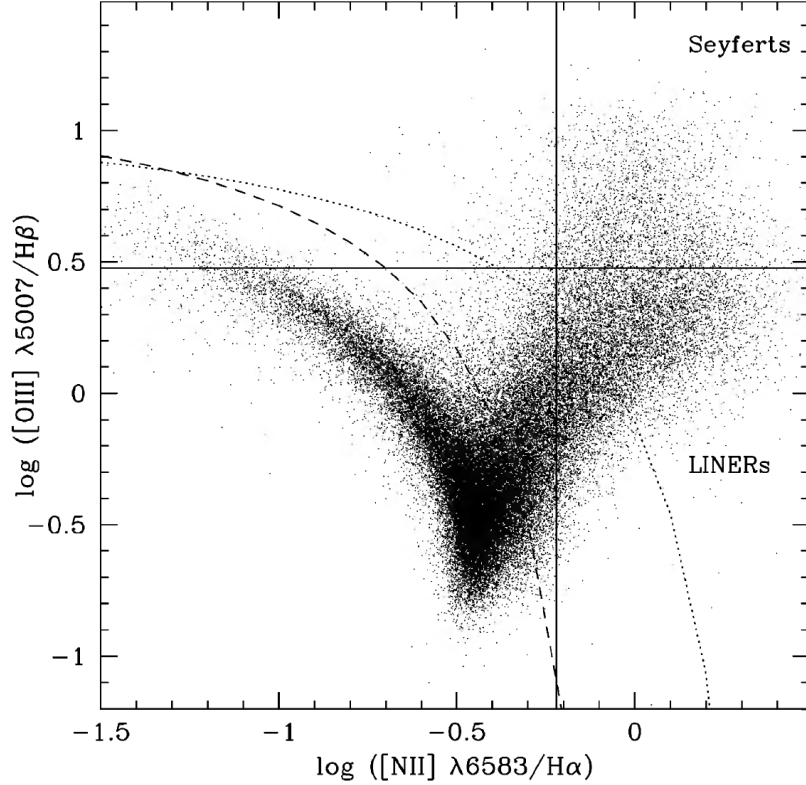


Figure 11: Example of a BPT diagram, where the dotted line represents the [Kewley et al. \(2001\)](#) curve and the dashed line corresponds to [Kauffmann et al. \(2003\)](#). The characteristic shape of the diagram has earned it the nickname "seagull", with the "left wing" predominantly consisting of star-forming galaxies and the "right wing" representing AGN. Credit: [Kauffmann et al. \(2003\)](#)

[Kewley et al. \(2001\)](#) derived a theoretical boundary, represented by [Equation 14](#), which defines an upper limit for SFGs based on photoionisation models (simulations predicting gas ionisation by different radiation sources). Subsequently, [Kauffmann et al. \(2003\)](#) analysed a significantly larger galaxy sample and proposed an empirical improvement of this boundary, given by [Equation 15](#).

$$\log([\text{OIII}]/\text{H}\beta) = 0.61/(\log([\text{NII}]/\text{H}\alpha) - 0.47) + 1.19 \quad (14)$$

$$\log([\text{OIII}]/\text{H}\beta) = 0.61/(\log([\text{NII}]/\text{H}\alpha) - 0.05) + 1.3 \quad (15)$$

This classification arises from the fact that in galaxies with normal SF, hydrogen is ionised by radiation from young, massive stars. In contrast, AGN ionise through a much more energetic radiation field, often referred to as a "harder" radiation field, resulting in the AGN showing higher ratios. Star-forming galaxies would then show more in the lower left corner, while AGN would mainly be in the upper right corner.

More recently [Stasińska et al. \(2006\)](#) refined the classification further, introducing a new curve ([Equation 16](#)), where y is $\log([\text{OIII}]/\text{H}\beta)$ and x is $\log([\text{NII}]/\text{H}\alpha)$.

$$y = (-30.787 + 1.1358x + 0.27297x^2) \tanh(5.7409x) - 31.093 \quad (16)$$

[Stasińska et al. \(2006\)](#) found that approximately 3 % of their AGN fall below the [Kauffmann et al. \(2003\)](#) line, while nearly 20 % of objects lie in the region between the [Stasińska et al. \(2006\)](#) and [Kauffmann et al. \(2003\)](#) boundaries. They suggest this is due to the presence of very weak AGN.

4.9 Green Valley diagram

The term Green Valley diagram was first used by Christopher Martin in 2005, and it describes an ultraviolet colour-magnitude diagram. The $u-r$ colour is chosen due to its sensitivity to small amounts of ongoing star formation, meaning that even emission from young stars (< 100 Myr) would be seen ([Salim, 2014](#)).

The name of the diagram comes from the presence of a wide, flat region in the graphs (Green Valley region), dividing the red sequence (RS) from the blue cloud (BC). The red sequence represents passive red galaxies with an older stellar population, while the blue cloud comprises star-forming galaxies.

In this thesis, we are going to use the predefined Green Valley region from [van Velzen et al. \(2021\)](#). The upper limit is defined as:

$$u - r(M_\star) = -0.40 + 0.25 M_\star. \quad (17)$$

We are going to make the width of the Green Valley region 0.2, meaning the lower limit is:

$$u - r(M_\star) = -0.40 + 0.25 M_\star - 0.2. \quad (18)$$

Some observations indicate that certain galaxies within the Green Valley region exhibit signs of recent AGN activity ([Yao et al., 2023](#)), which may be triggered by tidal disruption events (TDEs), whenever the supermassive black hole tears apart a star. These events might trigger radio emission as well as the formation of compact radio jets. We seek to find if compact galaxies in our sample exhibit similar behaviour and answer if these sources can be remnants of TDE.

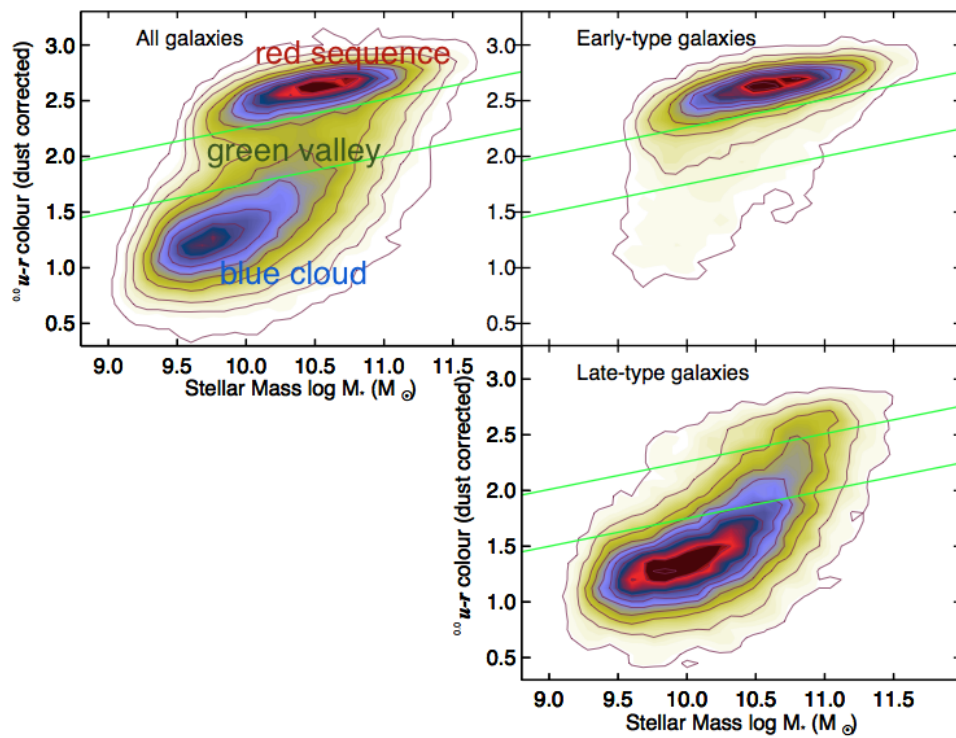


Figure 12: The Green Valley diagram showcases the division of red sequence and blue cloud, with the Green Valley region in between them. Credit: [Bruzual and Charlot \(2003\)](#)

5 Statistical methods - 1D and 2D KS tests

The KS test, named after Kolmogorov and Smirnov, is used to find whether two cumulative distribution functions (CDFs) come from the same distribution. The test is non-parametric, meaning the test does not need any specific parameters for the samples. We are going to focus on 1D and 2D KS tests.

5.1 1D KS test

One dimensional KS test compares an empirical CDF $S_N(x)$ of the sample, to the theoretical CDF $F_0(x)$ derived for a hypothetical sample. The theoretical CDF represents the expected distribution, while the empirical CDF represents the cumulative proportions of values in the sample, as mentioned in [Massey \(1951\)](#). The goal of the 1D KS test is to check how much the empirical CDF match the theoretical CDF, by evaluating the maximum difference D between the CDFs:

$$d = \max|F_0(x) - S_N(x)|. \quad (19)$$

If the difference is large, we can assume the sample does not match the theoretical CDF, indicating the hypothesis might not be correct ([Massey, 1951](#)).

We are going to use this test to evaluate if two different samples are from the same distribution. To do this, we will use the Python repository `KS_2SAMP`¹ from [1d \(2025\)](#), which will be able to calculate the maximum absolute difference (D) between the samples and the probability that the observed difference would be by chance (p -value), assuming the distributions are the same. The assumption is called the null hypothesis, and the p -value can tell us whether this assumption was correct or not. If the p -value is low (< 0.05), we can say that the two samples are different, which leads us to reject the null hypothesis. If the p -value is high (> 0.05), it signifies that the samples are not that different or that the null hypothesis is correct.

5.2 2D KS test

The 2D Kolmogorov-Smirnov test evaluates differences in spatial distributions, making it useful for datasets involving pairs of variables. This test uses the Monte Carlo method to evaluate the value of D as well as the p -value, meaning they are not exact but rather approximations. To calculate the 2D KS test, we used a Python code `NDTEST`² from [Syrte \(2025\)](#).

¹`KS_2SAMP`: https://docs.scipy.org/doc/scipy/reference/generated/scipy.stats.ks_2samp.html

²`NDTEST`: <https://github.com/syrte/ndtest>

6 The Roots of Data

In this section, we describe the data utilised in this thesis. We begin with an introduction to the catalogue of Radio sources associated with Optical Galaxies and having Unresolved or Extended morphologies (ROGUE), followed by a discussion of the outputs from the STARLIGHT spectral synthesis code. Additionally, we mention the data collected by the Infrared Astronomical Satellite (IRAS) mission.

6.1 ROGUE I/II

ROGUE was constructed by cross-matching spectroscopically identified galaxies from the SDSS (Sloan Digital Sky Survey) Data Release 7 with radio sources from FIRST (Faint Images of the Radio Sky at Twenty Centimetres) and NVSS (NRAO VLA Sky Survey) surveys. FIRST and NVSS were both observed using the VLA (Very Large Array), each with a different antenna configuration.



Figure 13: Antennas of the Very Large Array. Credit: [NRAO/AUI/NSF \(2025\)](#)

Both FIRST and NVSS were performed at 1.4 GHz frequency. However, due to the different antenna configuration, the FIRST survey captures images with an angular resolution of 5.4 arcsecs and is complete down to a flux density limit of 1 mJy, while NVSS identifies sources at 45 arcsecs and is complete down to 2.5 mJy. The difference in resolution and sensitivity makes the FIRST a better choice for detecting compact sources and the NVSS more reliable for identifying extended or diffused sources, due to the more compact array configuration.

The authors of the first part of the ROGUE catalogue containing radio galaxies with radio-emitting cores ([Kozieł-Wierzbowska et al., 2020](#)) identified the radio galaxies with radio cores by cross-matching the SDSS optical positions with the FIRST radio position of the source. Still, an error radius (δ_r) was considered as the surveys were carried out at different resolutions:

$$\delta_r = [((\alpha_{\text{SDSS}} - \alpha_{\text{FIRST}}) \times \cos \delta_{\text{SDSS}})^2 \cdot (\delta_{\text{SDSS}} - \delta_{\text{FIRST}})^2]^{1/2}, \quad (20)$$

where α is the right ascension and δ is declination. This error radius was calculated to be $\leq 3 \text{ arcsecs}$. If the centre of the radio source was within 3 arcseconds of the central component of the optical galaxy, the source was considered a match. After identifying the radio sources, an overlay of optical and radio maps was done to find the radio morphology of the sources, using a Digitised Sky Survey (DSS) and radio images from the FIRST and NVSS.

Radio morphology classification was done visually by the authors, for which they used the FIRST and the NVSS maps. The catalogue provides both NVSS and FIRST classifications separately. Nevertheless, due to the differing angular resolutions of the maps, the authors opted to use the map with more detailed features for the final classification.

The second part of the catalogue relaxed the separation to 3 arcsec to also include the sources without the radio core. The classification was carried out by the ROGUE team for all spectroscopically identified sources from SDSS dr7 by visually identifying the radio contours with optical host (for more details see Koziel-Wierzbowska et al. in prep.).

Extended sources with a minimum of two components were assigned classification based on [Fanaroff and Riley \(1974\)](#) (more details in [section 7](#)). The classification of single components itself is based on the deconvolved angular size. A two-dimensional Gaussian model was fitted to the observed element. In cases where deconvolution with the telescope beam yielded both minor and major axes of zero length, the source was considered unresolved and was classified as compact (C). If the deconvolved Gaussian resulted in at least one of the axes larger than zero, the source was classified as elongated (E).

The optical morphological classifications were performed utilising 120 arcsecs cutout images from SDSS, and the standard Hubble classification scheme was applied.

In this catalogue, there are a few cuts that should be mentioned. The cut for redshift is $0.0021 - 0.636$. Total radio luminosity was done at 1.4 GHz and the range is from $10^{18.86} \text{ WHz}^{-1}$ to $10^{26.59} \text{ WHz}^{-1}$, while the core radio luminosity is set from $10^{18.86} \text{ WHz}^{-1}$ to $10^{26.26} \text{ WHz}^{-1}$. The optical magnitude for sources in this catalogue is 17.77, and the flux density limit is 0.6 mJy using the FIRST survey.

Both ROGUE I & ROGUE II catalogues also provide several other calculated properties of the galaxies. To name a few, authors have calculated the luminosity distance (d_L), angular diameter distance (d_m), angular size, monochromatic radio luminosity (L_{obs}), optical magnitudes in SDSS filter bands (M_{band}) and more.

6.2 STARLIGHT

STARLIGHT is a spectral synthesis code developed to break down an observed galaxy spectrum into a mix of simple stellar populations that differ

in age and metallicity, utilising the models proposed by [Bruzual and Charlot \(2003\)](#). By analysing the observed spectra with this method, we can estimate some physical characteristics of the host galaxy.

The extraction of the fitted stellar spectrum from the observed one allows us to correct the observed emission line luminosities for the influence of the underlying stellar absorption. Results from the STARLIGHT fits to SDSS dr6 optical spectra are available as a supplementary material to the ROGUE, including the measurements of emission line luminosities, velocity dispersion, dust attenuation, star formation rate, stellar mass and more.

6.3 IRAS



Figure 14: Testing of IRAS in the Netherlands. Credit: [RAL Space \(2024\)](#)

The Infrared Astronomical Satellite (IRAS) was a joint mission by the United States, the United Kingdom, and the Netherlands. It operated for 10 months until November 21, 1983, carrying a 0.6 m Ritchey-Chrétien telescope cooled by liquid helium. During its mission, IRAS conducted an all-sky infrared survey at 12, 25, 60, and 100 microns, with an angular resolution ranging from $0.5'$ to $2'$ ([NASA Goddard Space Flight Center, 2024](#)).

The importance of this mission for us is in the measured fluxes at 60 and 100 microns, which we will use further in this work to calculate the FIR flux.

IRAS produced several catalogues, most importantly for us, the Point Source catalogue (PSC) and the Faint Source catalogue (FSC).

The PSC ([NASA HEASARC, 2024](#)) contains approximately 250,000 infrared point sources, with apparent sizes smaller than $0.5'$, $1.0'$, and $2.0'$ at different wavelengths. It provides source positions, flux densities, and various flags describing their properties.

The FSC ([NASA/IPAC Infrared Science Archive, 2024](#)) extends the survey to fainter sources, cataloguing around 593,000 objects. It is 2.5 times more sensitive than the PSC, allowing the detection and study of dimmer infrared sources.

7 Sample selection

A key question that we aim to answer is what distinguishes extended galaxies from compact ones. To investigate this, we selected both compact radio sources (C), which are unresolved at small angular sizes and various types of extended radio galaxies, including distorted radio sources and classical radio galaxies of Faranhoff Riley type.

Among distorted radio galaxies, we included one-sided FRI and FR II sources (OI, OII), as well as galaxies with distinct morphologies such as Z-shaped (Z), X-shaped (X) and double-double (DD) radio galaxies, which feature two pairs of lobes. We also chose narrow-angle tail sources with the angle between lobes $< 90^\circ$ (NAT) and wide-angle sources with the angle between lobes $> 90^\circ$ (WAT) as distorted galaxies. For FR galaxies, we selected FRI (I), FR II (II), and hybrid FR galaxies (I/II), where one lobe follows the FRI classification, while the other follows FR II. Additionally, all of these classifications can carry a “p” prefix, indicating uncertainty in their attribution. For consistency, in the following sections, we will be working only with galaxies of the mentioned morphologies.

The distinction between compact and subclassifications of extended galaxies was based on observations from the FIRST survey as presented in the ROGUE catalogue.

The optical morphology was taken from the SDSS survey and also presented in ROGUE. The division we took into account is into elliptical (E), distorted (D), spiral (S), and lenticular (L) galaxies.

In extended galaxies, the origin of the radio emission is clear, while determining the nature of the emission in compact sources is far more challenging, as both the unresolved jets and star-forming regions can contribute. High resolution radio observations obtained with VLBI are available only for a handful of objects. That is why we need to rely on the classification diagrams, such as DLM and BPT, but still with caution.

Throughout this thesis, we will refer to a galaxy as an AGN if it is classified as such by both the DLM and BPT diagrams. Galaxies identified as SF by the DLM diagram but not classified as SF by the BPT diagram will be referred to simply as Seyfert. If a galaxy is classified as star-forming by both diagrams, we will refer to it as SFG. In cases where a different classification is used, it will be explicitly stated. The results of the DLM diagram are discussed in more detail in [subsection 7.2](#), and the BPT diagram is described in [subsection 7.1](#).

We decided to study objects with a redshift cut $0.02 - 0.2$. All calculations, plots, and tables were generated using Python scripts developed by us. However, when matching the IRAS catalogues with our data, we performed the matching process using TOPCAT.

7.1 BPT diagram

First, we separated the galaxies into two groups based on their optical emission-line ratios. The ones that are consistent with star formation, and those that have ratios suggesting the presence of an optical AGN. Then we constructed the BPT diagram as explained in [subsection 4.8](#). We selected extended, compact, as well as elongated galaxies.

Generally, higher line ratios indicate a stronger AGN component, while lower ratios suggest dominance of star-forming galaxies. However, if we move closer to the central region of the plot, both star formation and AGN contribute to the observed ratios in a non-negligible way. Therefore, we need to rely on suggested separation lines. We adopt the line presented by [Stasińska et al. \(2006\)](#) to robustly identify the primary source, given its capability to distinguish even faint AGN.

In [Figure 15](#), we marked sources classified as star-forming by both the BPT and the DLM diagrams (discussion of the DLM is in [subsection 7.2](#)) as blue points. Green and yellow points represent sources hosting optical AGN. While green points are classified as AGN only by the BPT diagram, yellow points represent AGN classification by BPT as well as the DLM diagram. In the BPT diagram, we included only those objects for which all lines had a signal-to-noise ratio $\text{SNR} \geq 5$.

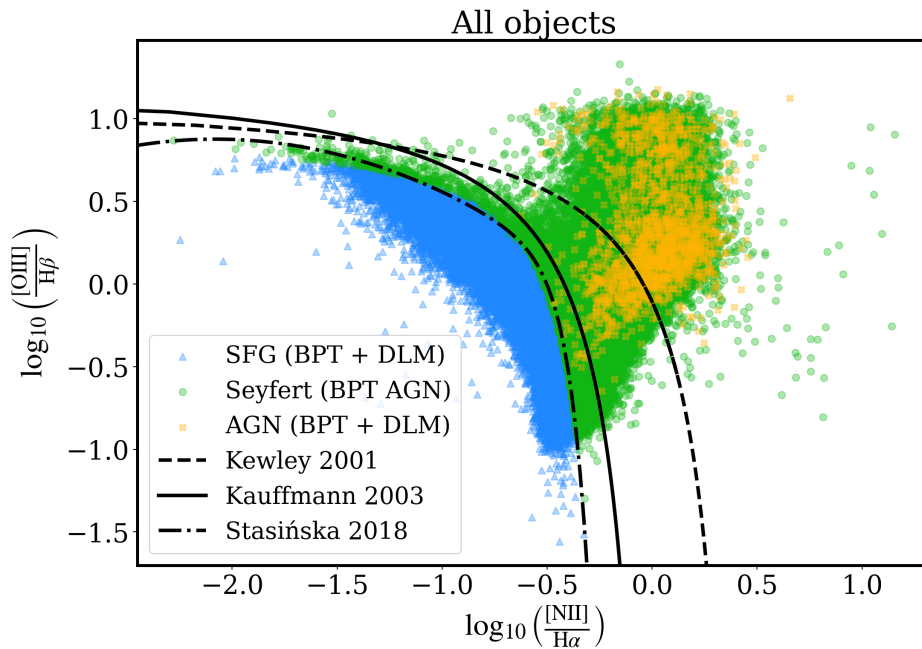


Figure 15: BPT diagram, with division based on the [Stasińska et al. \(2006\)](#) line. Green and yellow points mark sources with optical AGN and while green points represent AGN classified only by the BPT diagram, yellow ones are also classified as AGN by the BPT diagram. Blue points are star-forming galaxies classified by both the BPT and DLM diagrams.

7.2 DLM diagram

The DLM diagram, described in [subsection 4.4](#), is commonly used to identify the dominant source of radio emission. Whether the output is primarily driven by the AGN outflows, or rather by the star-forming process in the host galaxy.

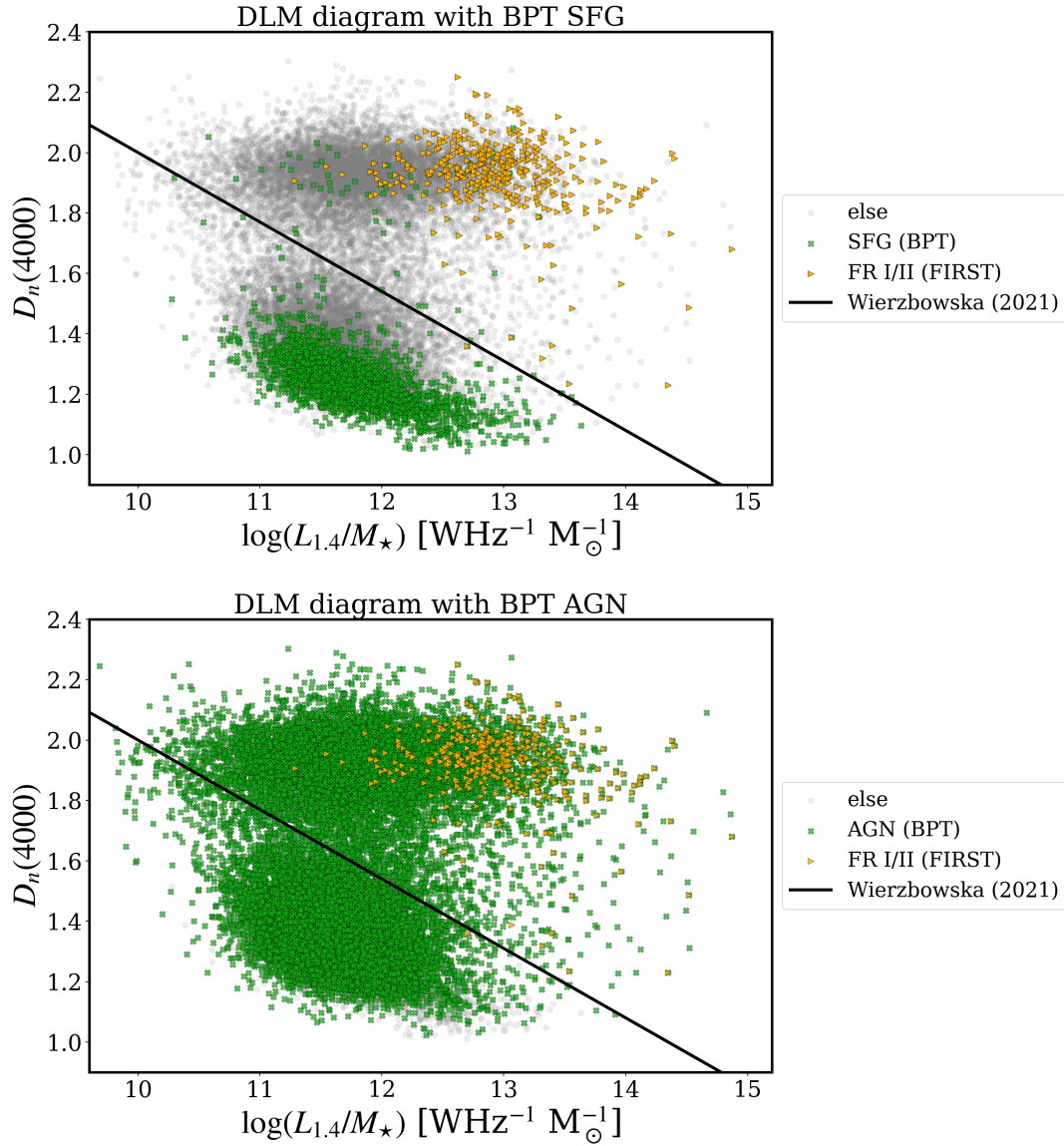


Figure 16: DLM diagram using the ROGUE data, highlighting FR I and FR II with yellow colour, along with SFRs (upper diagram) and AGN (lower diagram) according to the BPT diagram only in green.

In [Figure 16](#) we present the DLM diagram constructed using data from the ROGUE catalogue, marking the position of FR I and FR II galaxies with yellow and optical AGN and SFGs identified via the BPT diagram with green.

While the optical AGN are distributed all over the diagram, SF galaxies identified on the BPT diagram cluster in the lower left corner of the DLM diagram. FRI and II concentrate in the upper right corner. It indeed seems that the upper branch of the DLM diagram corresponds to radio emission dominated by the AGN outflows. We ask to see if the lower branch, believed to have emission dominated by the host galaxy, might contain a weak radio signal from AGN. This issue and radio excess are further discussed in [subsection 7.3](#).

7.3 FIR and total radio luminosity

FIR-radio luminosity correlation is one of the most robust methods to identify whether the emission of the source is consistent with star formation, or if there might be some radio excess hinting towards the presence of radio AGN/outflows. We applied this method to galaxies classified as star-forming based on the DLM diagram, but with line ratios of the BPT diagram implying the presence of an optical AGN (Seyfert galaxies). We aim to find if these sources have radio emission dominated by the host galaxy or AGN, and if so, then to what extent.

To investigate the relationship between FIR and radio luminosity, we began by cross-matching sources from the ROGUE catalogue with the IRAS database. We used TOPCAT³ software to do so. Coordinates were considered a match if the object’s separation was no greater than 5.4 arcsec , corresponding to the resolution of the FIRST beam. Our sources were mostly identified in the PSC and FSC IRAS catalogues, so we only included those.

In the next step, we filtered these galaxies to select only those classified as Seyferts based on BPT diagnostics, in order to investigate whether their radio luminosity originates from AGN activity. In addition to compact and extended sources, we also included elongated sources to enlarge this sample.

To estimate FIR luminosity, we used flux densities at $60 \mu\text{m}$ and $100 \mu\text{m}$ from IRAS and applied the relations given in [Equation 11](#) and [Equation 10](#). Since the flux density values also came with quality flags, we only kept sources where both values had a quality rating of at least 2 (moderate) or 3 (high).

We also estimate the q factor from [Equation 13](#). In [Figure 17](#) we present the FIR-radio luminosity correlation, for ROGUE galaxies found in the PSC or FSC catalogues. We see that the majority of sources do not deviate from the correlation obtained for SF galaxies ([Yun et al. \(2001\)](#) claimed it is $q = 2.34$), as also seen in [Figure 18](#). Many sources seem to have brighter FIR than expected given their radio luminosity at 1.4 GHz. We note that the IRAS has lower resolution than FIRST, which might lead to FIR emission contamination by nearby objects. We also found that a few objects show some form of radio excess deviating from the mean value by more than one sigma.

³TOPCAT: <https://www.star.bris.ac.uk/~mbt/topcat/>

We aim to calculate the fractional contribution of star-forming regions to total radio emission at 1.4 GHz. The optical spectra in ROGUE are fitted by STARLIGHT, the spectral synthesis code. This code can estimate the sSFR and, applying the [Murphy et al. \(2011\)](#) relation ([Equation 8](#)), we can calculate the expected radio luminosity associated purely with star forming regions ($L_{1.4, \text{SFR}}$). The SFR was derived using the sSFR and M_* , keeping in mind the relation given in [Equation 1](#).

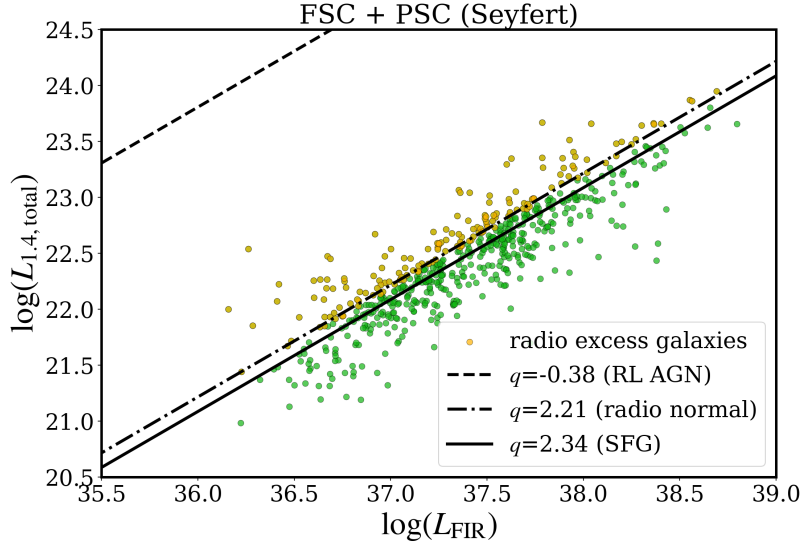


Figure 17: The FIR vs. total luminosity at 1.4 GHz $L_{1.4, \text{total}}$ of Seyfert objects with FSC or PSC data, alongside the lines representing the q factors mentioned in [subsection 4.5](#). Yellow points mark galaxies with radio excess ($q < 2.24$ is the mean value for SF galaxies minus the error).

[Figure 18](#) shows the fractional contribution of radio emission from SFR ($L_{1.4, \text{SFR}}$) to total radio luminosity at 1.4 GHz ($L_{1.4, \text{total}}$) as a function of q factor. The colour scale depicts the visual extinction of the light in the V -band, which is due to the presence of the dust attenuation in the host galaxy (A_V). It is important to mention that SFR was estimated solely by optical spectra modelling using the STARLIGHT code, which implies that in cases of strong dust attenuation within the host galaxy, the SFR derived from STARLIGHT may be significantly underestimated.

We see that the majority of our selected sources exhibit a low $L_{1.4, \text{SFR}}/L_{1.4, \text{total}}$ ratio, even if the q factor is consistent with radio emission originating in SF regions. However, we note that sources that are around $L_{1.4, \text{SFR}}/L_{1.4, \text{total}} \approx 0$, exhibit higher A_V parameter, which may imply that the SFR calculated using STARLIGHT is underestimated, which could also result in the underestimation of the $L_{1.4, \text{SFR}}$. If one attempts to correct the total radio luminosity using our method, by subtracting the contribution from SF regions using the [Equation 8](#), the result represents rather the upper limit of the radio luminosity from AGN. Generally, the contribution of SFR to total radio

emission increases as we go to higher q factor values. If the selected SF objects had the q -factors consistent with radio dominated by SFR, then by adopting the [Murphy et al. \(2011\)](#) relation, we should obtain $L_{1.4, \text{SFR}}/L_{1.4, \text{total}} \approx 1$, not 0. Still, the general trend is well reflected as the sources seem to have higher ratios $L_{1.4, \text{SFR}}/L_{1.4, \text{total}}$ for higher q factors.

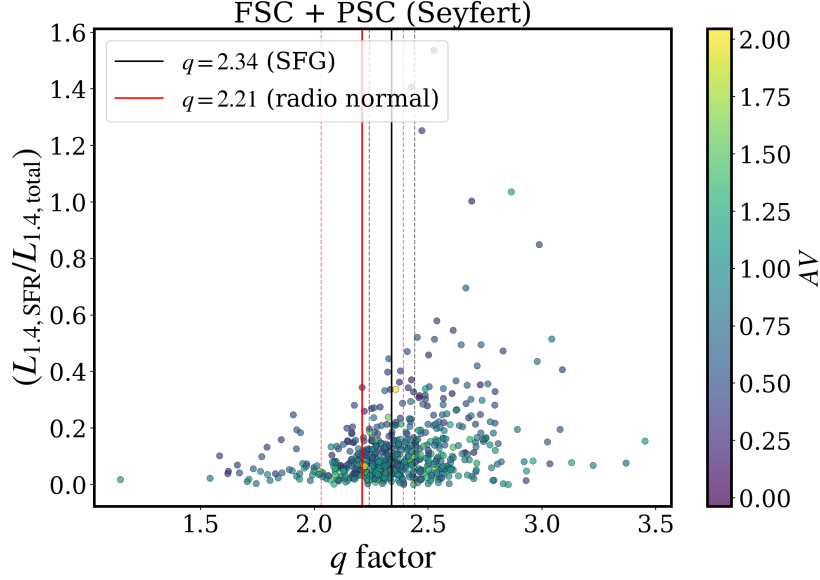


Figure 18: Calculated q factor vs. $L_{1.4, \text{SFR}}/L_{1.4, \text{total}}$ of compact objects classified as Seyfert with FSC/PSC data, with colour map of A_V . The red line corresponds to $q = 2.21$ of radio normal galaxies, and the black line is for SFG with $q = 2.34$. Dashed lines represent their sigma errors.

In [Figure 19](#), we present the DLM diagram once again. This time, we also indicate the position of radio sources detected in PSC/FSC databases. As we can see, the majority of these sources are located in the lower left corner, where SF galaxies reside. We also marked the location of the sources that we identified as radio excess ($q < 2.24$). We do not see any clear separation of these sources on the DLM diagram, however, a few radio excess sources fall into the AGN part of the plot.

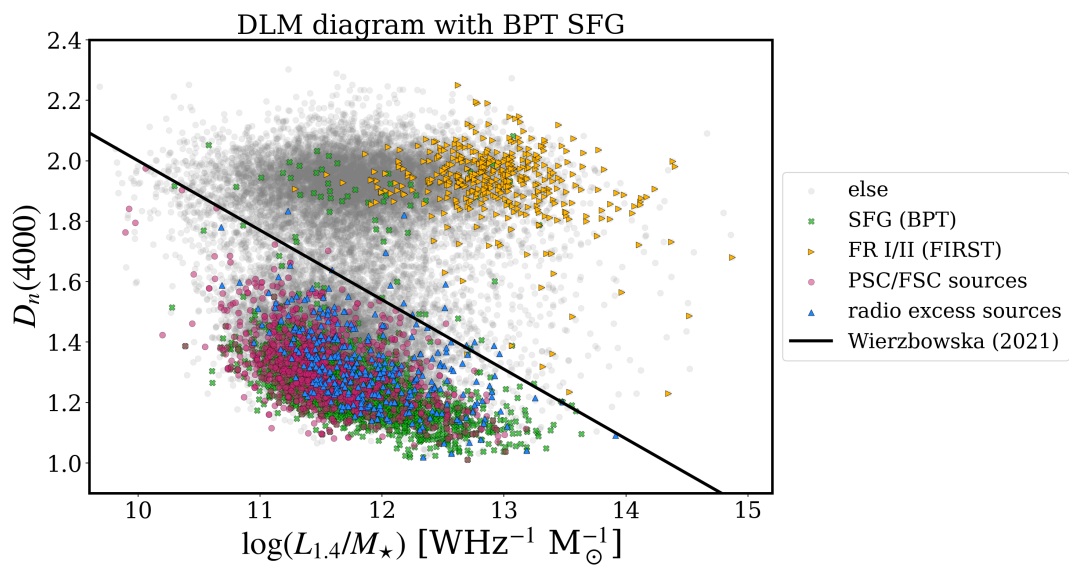


Figure 19: DLM diagram using the ROGUE data, with FRI and FR II marked with yellow and SFG according to the BPT diagram only with green. Pink represents the PSC/SFC data. Additionally, sources with radio excess ($q < 2.24$ is the mean value for SF galaxies minus the error) are marked with blue.

8 Analysing the data

In this section, we are going to analyse the data selected from the ROGUE catalogue, using the methods described in [section 7](#). In the following subsections, we attempt to understand why some radio galaxies do not form extended structures. We divide the sources into AGN (according to the DLM diagram), and as some Seyfert galaxies show radio excess, we also include those objects in our analyses. These Seyfert galaxies are DLM SF; however, line ratios on the BPT diagram imply the presence of optical AGN. We show each class in a separate plot.

8.1 Linear size

Since compact radio galaxies are single-component objects with measured angular sizes that do not exceed the resolution of FIRST, the deconvolved angular sizes result in zero. That is why for these objects we adopted the FIRST beam size of 5.4 arcseconds, which serves as the upper limit of their angular sizes. We note that the values are probably significantly overestimated.

To calculate the linear size, we adopted the same values of cosmological parameters as were used in the ROGUE catalogue, with $H_0 = 69.6$ km/s/Mpc, $\Omega_M = 0.286$, and $\Omega_\Lambda = 0.714$. Establishing the cosmology is crucial for getting the distance to the source, which is needed to measure the linear size and luminosities of galaxies. We determined the angular diameter distance (d_m) of the sources using the Python version of the cosmology calculator ⁴ from [Wright \(2006\)](#) and using the redshifts provided in the ROGUE catalogue. The linear size was estimated from the [Equation 21](#), where the angular size was taken from the ROGUE or, for compact sources, taken as the FIRST beam size.

$$\text{linear size} = \text{angular size} \cdot d_m \cdot \frac{\pi}{648000} \quad (21)$$

[Figure 20](#) shows total luminosity at 1.4 GHz ($L_{1.4, \text{total}}$) as a function of linear size, separately for AGN and Seyfert galaxies. Linear sizes of compact sources, marked with green, remain similar between the two groups, for the redshift cut mentioned in [section 7](#). The total radio luminosity of compact sources appears to be smaller for Seyfert galaxies than for AGN. For AGN compact galaxies, the lower quantile is $q_{0.2} = 22.462$ and the upper quantile is $q_{0.8} = 23.256$, while for compact Seyfert galaxies $q_{0.2} = 22.014$ and $q_{0.8} = 22.824$.

Almost no FR or distorted morphologies are found among Seyfert, other than 3 distorted galaxies. However, many extended sources are found among the AGN. These sources typically have large linear sizes as well as high 1.4 GHz radio luminosity. The lower and upper quantiles of radio luminosity of FR AGN sources are $q_{0.2} = 23.959$ and $q_{0.8} = 24.754$. Similarly, distorted galaxies have upper quantile $q_{0.2} = 23.938$, and lower quantile $q_{0.8} = 24.676$.

⁴COSMOLOGY CALCULATOR: <https://www.astro.ucla.edu/~wright/CosmoCalc.html>

This implies that the distributions of FR and distorted galaxies are similar but higher than those for compact sources.

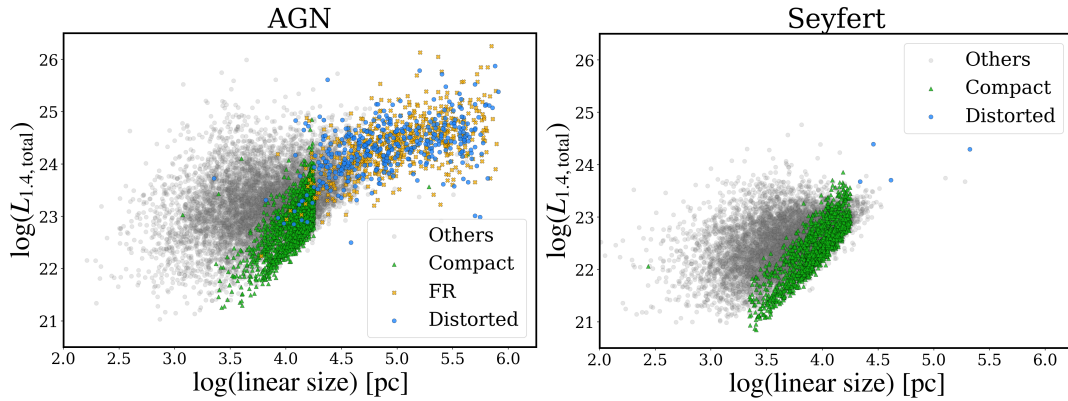


Figure 20: Linear sizes vs. total luminosity at 1.4 GHz $L_{1.4, \text{total}}$ diagram. Green represents compact sources, blue points are distorted sources, while yellow represents FR galaxies.

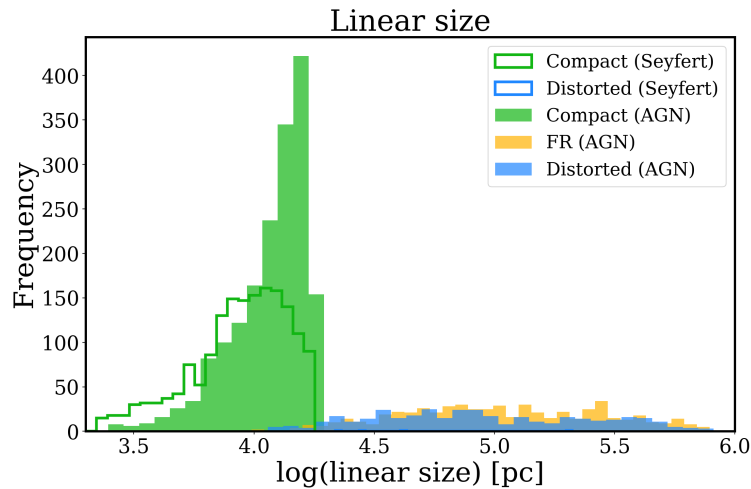


Figure 21: Distribution of the linear sizes of AGN and Seyfert galaxies. Filled green columns represent AGN, while borders are Seyfert galaxies.

In [Figure 20](#) we also indicate the positions of elongated galaxies (grey points), which seem to cluster towards smaller linear sizes. This phenomenon is anticipated since their deconvolved angular sizes are naturally smaller than the beam size used as the angular size for compact sources. It is worth noting that, for these elongated sources, the actual physical size might be underestimated due to resolution constraints. Conversely, compact sources are probably much smaller than the size suggested by using the FIRST beam size as their angular size.

8.2 Host galaxy properties

In the following subsection, we analyse the properties of optical host galaxies. We aim to determine if the properties of galaxies hosting compact radio AGN vary from those that accommodate extended radio AGN. Additionally, we provide the parameter distributions for our Seyfert galaxy sample for a better comparison. The findings are presented in more detail in the following subsection.

8.2.1 Redshift distribution

Figure 22 shows the redshift (z) distribution of Seyfert and AGN divided into compact, distorted and FR galaxies. We can see that no division has a predominant peak, however, compact Seyfert galaxies seem to peak at a smaller redshift than compact AGN. This is the result of different luminosity functions for Seyfert galaxies and AGN. The luminosity function of Seyfert galaxies peaks at low luminosity (Ermash, 2013), while for AGN, the luminosity function remains relatively flat (Tempel et al., 2011). As a consequence, the number of identified Seyfert galaxies decreases rapidly with increasing redshift.

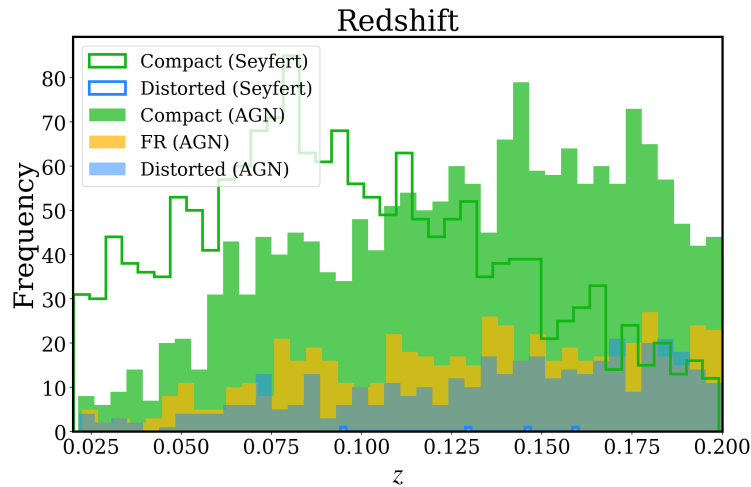


Figure 22: Redshift (z) distribution of Seyfert galaxies (borders) and AGN (filled columns).

8.2.2 Optical morphology

In this section, we present the optical morphologies of host radio galaxies with a division into compact, elongated, distorted and classical FR radio morphologies.

First, in Figure 23 we plot the morphologies of the Seyfert galaxies to provide a basis for comparison with the sources we identified as radio AGN.

We confirmed that only three distorted galaxies and no FR galaxies were present in the Seyfert sample. All subclasses of Seyfert galaxies typically host distorted galaxies, followed by spiral, lenticular and then elliptical galaxies, which have the smallest representation. Nonetheless, the Seyfert sample includes a significant representation of all the Hubble morphological types.

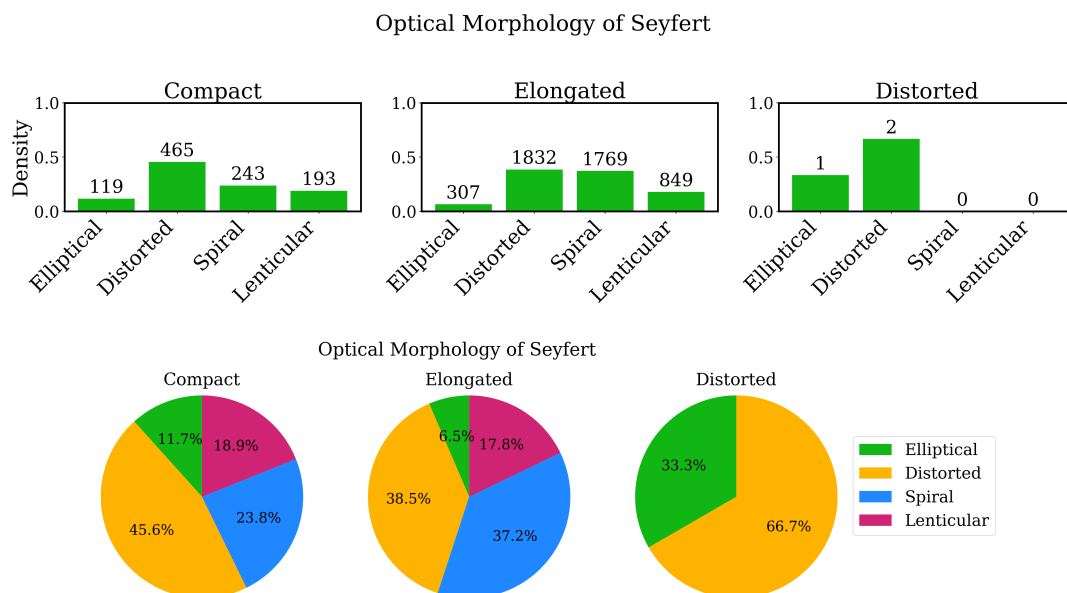


Figure 23: Density histograms and pie charts of optical morphology for Seyfert galaxies with numbers of objects in each group. Division is into elliptical, distorted, spiral and lenticular galaxies. No FR galaxies were found.

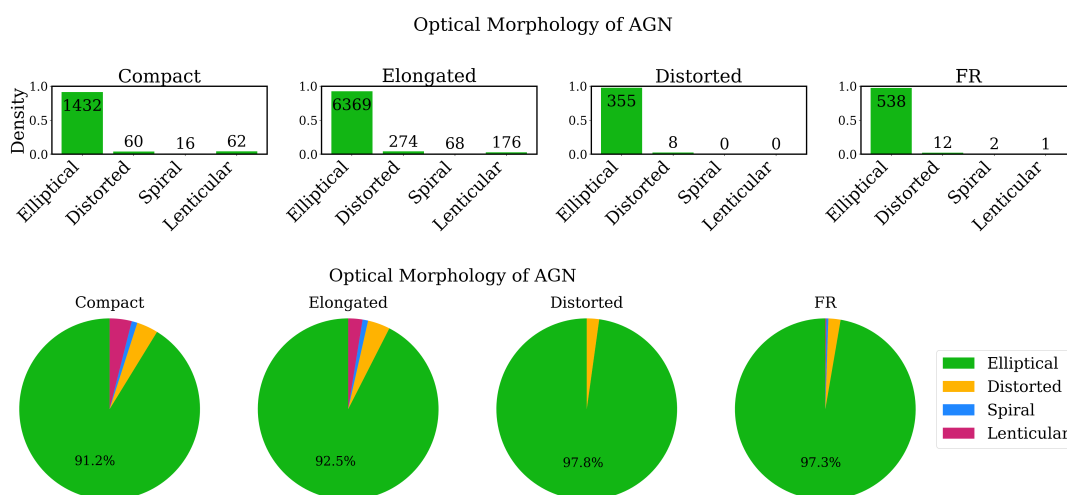


Figure 24: Density histograms and pie charts of optical morphology for AGN with numbers of objects in each group. Division is into elliptical, distorted, spiral and lenticular galaxies.

The optical morphologies of host galaxies for the AGN sample were plotted in Figure 24. It is evident that elliptical galaxies dominate across all radio morphologies. When comparing extended and compact sources, we find that elliptical galaxies in extended sources represent about 97.8 – 97.3%, while in compact sources the percentage is significantly smaller (91.2%). Compact sources also have a higher fraction of lenticular galaxies (3.9%), which is not that common for extended sources (distorted have no lenticular galaxies, while FR only one in the whole sample).

8.2.3 Stellar Mass

The total stellar mass (M_*), plotted in Figure 25, is generally bigger for AGN than for Seyfert galaxies, with FR and distorted AGN having the highest and compact Seyfert galaxies having the smallest stellar mass.

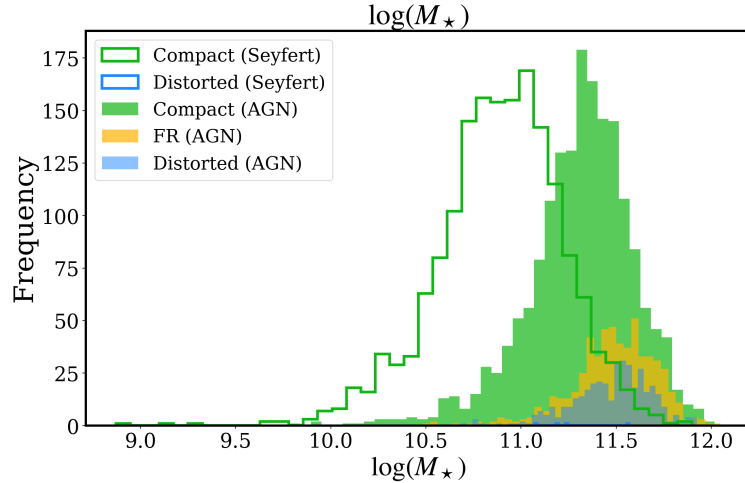


Figure 25: Total stellar mass (M_*) distribution of Seyfert galaxies (borders) and AGN (filled columns).

To better quantify the difference between the population of extended AGN and compact AGN, we performed the KS test to check if our two samples might be from the same distributions. We adopted the significance level $\alpha = 0.05$.

By applying the KS test to compact AGN vs. extended AGN galaxies, we obtained $p\text{-value} = 7.406 \cdot 10^{-52}$ and test statistic $D = 0.306$. The p -value smaller than the significance level implies that we can confidently say that the distribution of the stellar mass is different for compact and extended sources. Indeed, if we look at the Figure 25, we can see that compact AGN generally have smaller stellar masses than extended sources, while their stellar mass distribution is also shifted closer to the values characteristic for Seyfert galaxies from our sample.

8.2.4 Dust attenuation and Balmer decrement.

This section is going to discuss the dust properties within the host galaxy.

As mentioned in subsection 4.6, the $A_{V,Balmer}$ parameter informs us about the dust affecting the ratio of the Balmer emission lines. This results from dust attenuation along the line of sight within the narrow line region in the dusty torus and interstellar medium of the host galaxy. In Figure 26 we show that in the case of extended sources, no clear maximum is distinguishable. However, we note that $A_{V,Balmer}$ could be obtained only for a few sources, since generally no prominent Balmer emission lines are observed in extended sources. For compact AGN sources, the maximum at around $A_{V,Balmer} = 0.5$ was identified, while the maximum for Seyfert galaxies is shifted towards higher values $A_{V,Balmer} = 2.1$.

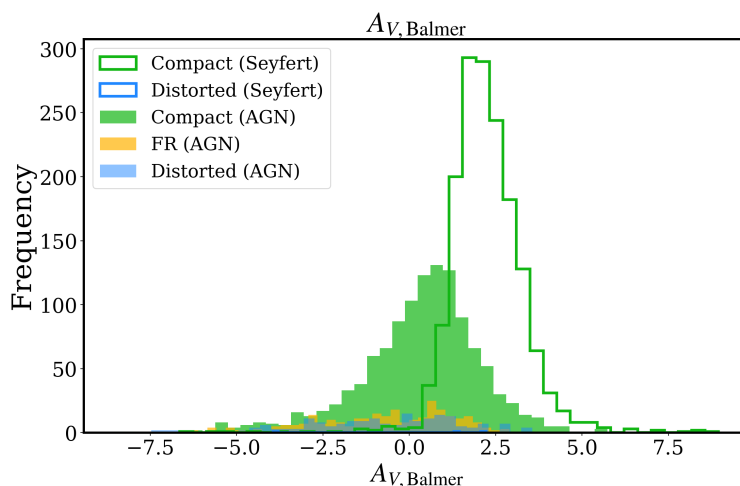


Figure 26: $A_{V,Balmer}$ parameter distribution of Seyfert galaxies (borders) and AGN (filled columns).

This suggests that while in the extended galaxies the amount of dust varies and oscillates around $A_{V,Balmer} \sim 0$, compact galaxies show consistently little higher dust extinction, no matter whether the compact galaxy is classified as AGN or Seyfert. Still, the dust attenuation in compact galaxies is not as significant as for Seyfert galaxies, and thus, these systems have generally less dust.

The effect on the dust by the Balmer decrement results in bluer frequencies being absorbed, so the negative values of $A_{V,Balmer}$ are not physical. However, as shown in Figure 26, the $A_{V,Balmer}$ parameter reaches negative values for some of the sources. This might be due to the measurement uncertainties or fitting procedures that wrongly estimated the value as negative.

We quantify if the plotted difference in $A_{V,Balmer}$ among compact and extended AGN is significant by performing the KS test. We obtained results $p\text{-value} = 1.168 \cdot 10^{-18}$ and $D = 0.2460$, which confirms that the difference is in fact significant.

As $A_{V,\text{Balmer}}$ could not be measured in all of our sources, we supplement this analysis by plotting the distribution of A_V obtained by fitting the composite stellar population with STARLIGHT assuming [Cardelli et al. \(1989\)](#) reddening law. The obtained values of the A_V are plotted in [Figure 27](#).

The A_V values for AGN oscillate around $A_V \approx 0$, and Seyfert galaxies have values of A_V peaking around $A_V \approx 0.8$, meaning that the Seyfert galaxies do in fact higher dust fraction than AGN. It also seems that the compact AGN have slightly higher A_V values than extended AGN. The KS test results for compact and extended AGN imply that this difference is indeed significant, as the p -value = $4.552 \cdot 10^{-47}$ and $D = 0.292$.

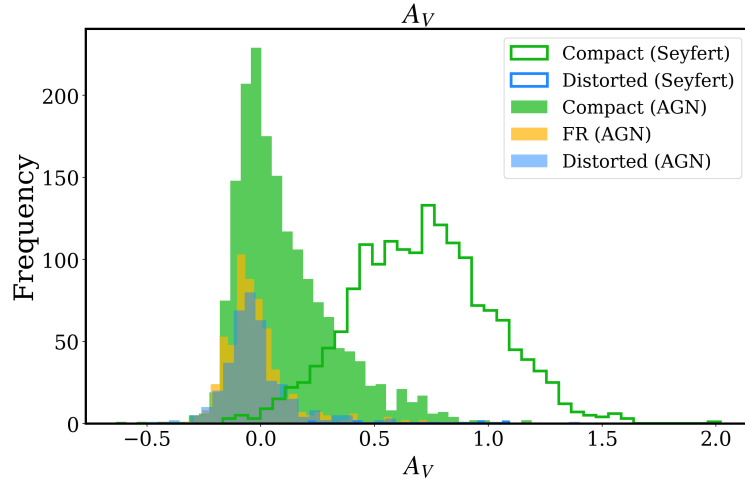


Figure 27: A_V parameter distribution of Seyfert galaxies (borders) and AGN (filled columns).

8.2.5 Starformation rate

In [Figure 28](#) we show the distribution of star formation rates among studied sources. It is evident that compact Seyfert galaxies have the highest SFR, which is consistent with their classification as SF according to the DLM diagram. FR galaxies and distorted AGN galaxies show almost no difference in their distribution, while compact AGN seem to have, on average, a bit smaller values of SFR.

The significance of the difference in distribution of SFR was confirmed by the KS test. Analysing the SFR of compact and extended AGN, we obtained $p = 3.0887 \cdot 10^{-9}$ and $D = 0.146$ ([Figure 28](#)).

SFR measures the total number of stars formed in a year interval. Naturally, in more massive galaxies, the SFR can be a little higher, since there is more dust and gas for the formation of stars. The specific star formation rate (sSFR) accounts for this dependency and is defined as the SFR normalised by the stellar mass of the galaxy ([Equation 1](#)), which can tell us about the efficiency

of the star formation relative to the mass of the galaxy. The sSFR distribution is in Figure 29 and follows a similar trend as Figure 28, where Seyfert galaxies have the highest sSFR.

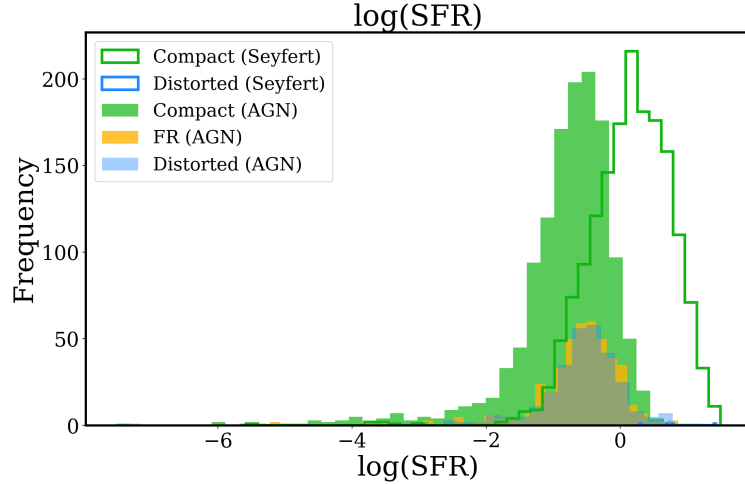


Figure 28: SFR distribution of Seyfert galaxies (borders) and AGN (filled columns).

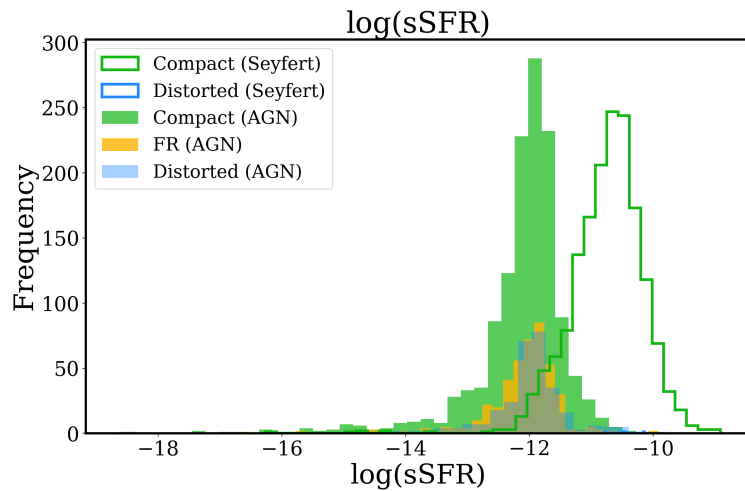


Figure 29: sSFR distribution of Seyfert galaxies (borders) and AGN (filled columns).

The result of the KS test on sSFR, on the other hand, indicates no significant difference between the two samples, with p -value = 0.326 and KS statistic $D = 0.043$, as also illustrated in Figure 29.

To summarise, we found that there is a significant difference in the distributions of star formation rate (SFR) and the galaxy's stellar masses (M_*). Still, specific star formation rate (sSFR) is not significantly different.

8.3 AGN properties

In [Figure 30](#) we show the position of AGN classified as having distorted, FR-like and compact radio morphologies on the BPT diagram. We can see that all the classified galaxies are above the [Stasińska et al. \(2006\)](#) line. The majority of the objects are also above the [Kewley et al. \(2001\)](#) line, which reinforces that the AGN is the dominant source of ionisation. We do not observe clustering or any sort of separation between the compact and extended sources.

To confirm this, we performed the 2D KS test for compact and extended galaxies and found that the p -value is 0.0643 and the D value is 0.192. The p -value is just above the threshold of 0.05, suggesting that these two samples are likely to be from the same distribution. However, we would need a bigger sample to further confirm this finding.

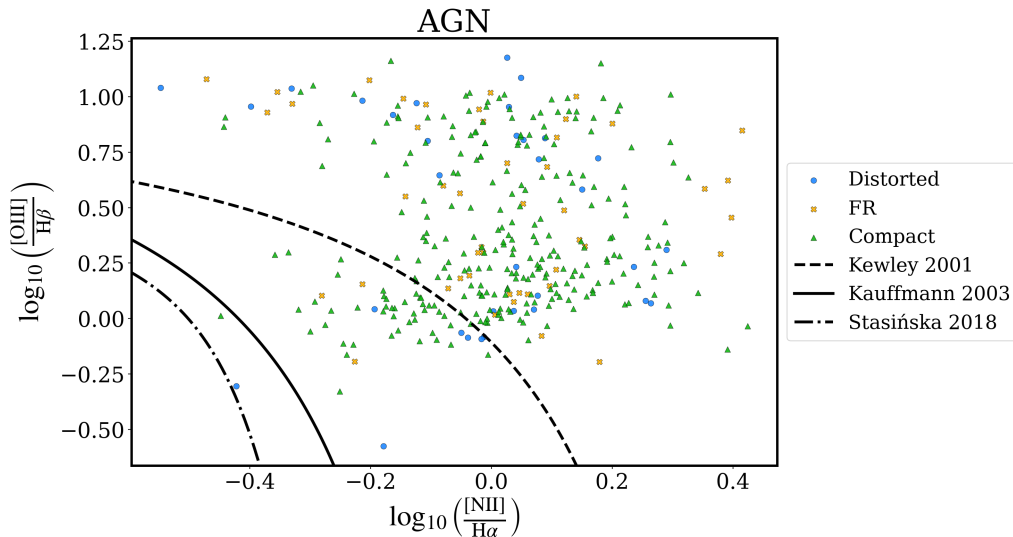


Figure 30: BPT diagram of compact, FR and distorted AGN galaxies.

8.3.1 Eddington and bolometric luminosity

The total amount of radiation that is emitted by the AGN at all wavelengths is measured by the bolometric luminosity. However, this requires observations at multiple wavebands, which is not always possible. Therefore, it is crucial to rely on the existing scaling relations that link measured quantities with the total bolometric luminosity. Two of these methods use either the $H\alpha$ line or the [OIII] emission line, which are believed to be excited by the AGN.

To estimate the bolometric luminosity from the $H\alpha$ line, we used [Equation 5](#), and for the luminosity calculated from [OIII] line we used [Equation 6](#).

We note that when an AGN is relatively weak, the impact of star-forming regions on the observed emission lines is substantial and cannot be ignored. [Stasińska et al. \(2025\)](#) addressed this issue by employing CLOUDY modelling.

This process involved accurately modelling the optical spectra and evaluating the source’s position on the BPT diagram to estimate the fractional contribution of both star-forming regions and AGN to observed luminosities of the lines. These values were then utilised to determine which of the two mentioned methods for computing the bolometric luminosity serves as a better proxy for the underlying AGN bolometric luminosity.

The comparisons of calculated luminosities from $H\alpha$ and $[OIII]$ to modelled ones are shown in [Figure 31](#). Since the line equivalent width $EW = 3 \text{ \AA}$ works as a suitable threshold for determining the main source of photoionisation, we decided to follow it in all the further plots and mark $EW > 3 \text{ \AA}$ as filled columns and $EW \leq 3 \text{ \AA}$ with borders.

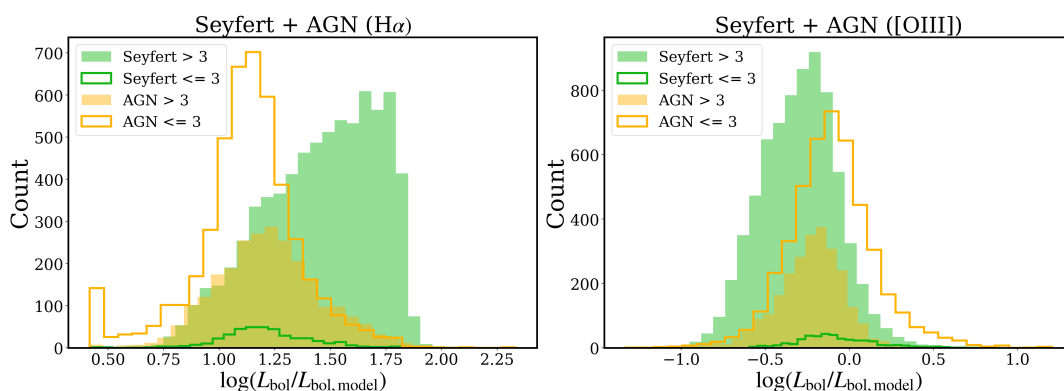


Figure 31: Histograms of the ratio of calculated bolometric luminosity (L_{bol}) using luminosity of $H\alpha$ ([Equation 5](#)) and $[OIII]$ line ([Equation 6](#)) to modelled bolometric luminosity ($L_{bol, model}$) for Seyfert galaxies and AGN. Filled columns represent objects with equivalent width over 3 \AA while borders represent objects with equivalent width smaller than or equal to 3 \AA .

In [Figure 31](#), we can see that the bolometric luminosities calculated via $H\alpha$ emission line are mostly overestimated with respect to values obtained by CLOUDY modelling, while the calculations based on the $[OIII]$ line are slightly underestimated. Still, the $[OIII]$ line serves as a better proxy, which is why we decided to work with this one in further analysis.

In [Figure 32](#) we plotted the Eddington ratio distribution of selected objects divided into two categories: Seyfert galaxies and AGN. We also marked the Eddington ratio $\lambda = 0.01$ with a vertical line. This can give us an understanding of the kind of accretion disk that is present within the host galaxy. Columns filled in indicate objects with $EW > 3 \text{ \AA}$, whereas borders signify $EW \leq 3 \text{ \AA}$.

The distribution of compact Seyfert galaxies with $EW > 3 \text{ \AA}$ peaks at around $\log(\lambda) = -2$, corresponding to the transition between the radiatively efficient Shakura-Sunyaev accretion disk and radiatively inefficient ADAF. This distribution is rather smooth (the quantile of 0.2 is $q_{0.2} = -2.593$ and

$q_{0.8} = -1.600$). The AGN, on the other hand, have values shifted toward the lower Eddington ratio $\log(\lambda) < -2$, implying the radiatively inefficient accretion flow, as given by the ADAF solution. Among the AGN, many sources have $EW \leq 3 \text{ \AA}$, suggesting that the emission is dominated by the HOLMES. However, we note that if $EW \sim 3 \text{ \AA}$, the contribution of the AGN is estimated to be still between 33 – 66%.

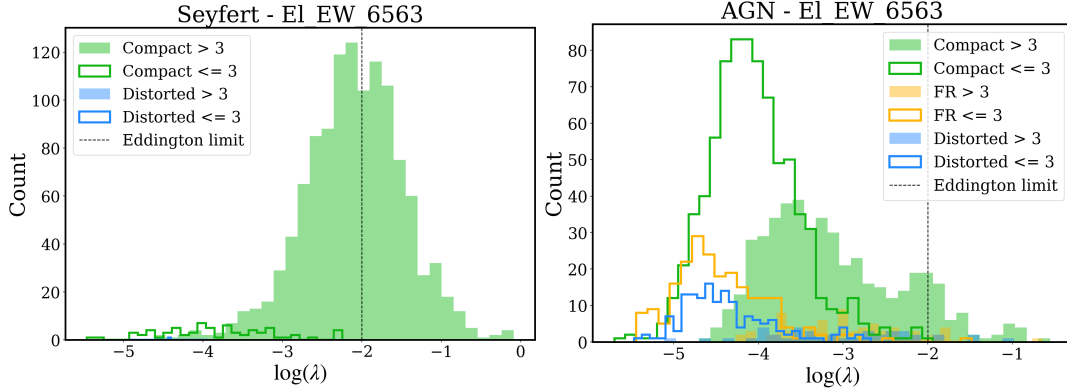


Figure 32: Histogram of the Eddington ratio (λ) of Seyfert galaxies and AGN. Bolometric luminosity (L_{bol}) used for the λ was calculated from the [OIII] line. Filled columns represent objects with equivalent width over 3 \AA while borders represent objects with equivalent width smaller than or equal to 3 \AA .

The KS test was performed on the AGN compact vs. extended sources with $EW > 3 \text{ \AA}$. We found that $p\text{-value} = 0.022$ and $D = 0.155$. The $p\text{-value}$ is slightly below the threshold of 0.05, meaning the two samples are probably not from the same distribution and the difference is significant. We also performed the KS test on the AGN compact vs. extended sources with $EW \leq 3 \text{ \AA}$. The results are $p\text{-value} = 8.167 \cdot 10^{-94}$ and $D = 0.685$. This $p\text{-value}$ is much smaller than the significance level, suggesting that for $EW \leq 3 \text{ \AA}$ there are two different distributions for compact and extended sources, and thus the difference is statistically confirmed.

The plot of black hole mass (M_{BH}) vs. the Eddington ratio (λ) is shown in [Figure 33](#). We can see that Seyfert galaxies generally have smaller black hole masses (M_{BH}), while AGN have more massive black holes. Extended sources are more concentrated in the upper left corner of the plot, towards the higher BH masses and lower Eddington ratios.

The 2D KS test for compact vs. extended AGN sources with $EW > 3 \text{ \AA}$ ([Figure 33](#)) revealed that $p\text{-value} = 7.23 \cdot 10^{-06}$ and $D = 0.294$, leading to conclusion on two different distributions for these groups. The same KS test was applied on sources with $EW \leq 3 \text{ \AA}$, with results $p\text{-value} = 5.38 \cdot 10^{-21}$ and $D = 0.360$, so there is a difference in distributions also for sources with $EW \leq 3 \text{ \AA}$.

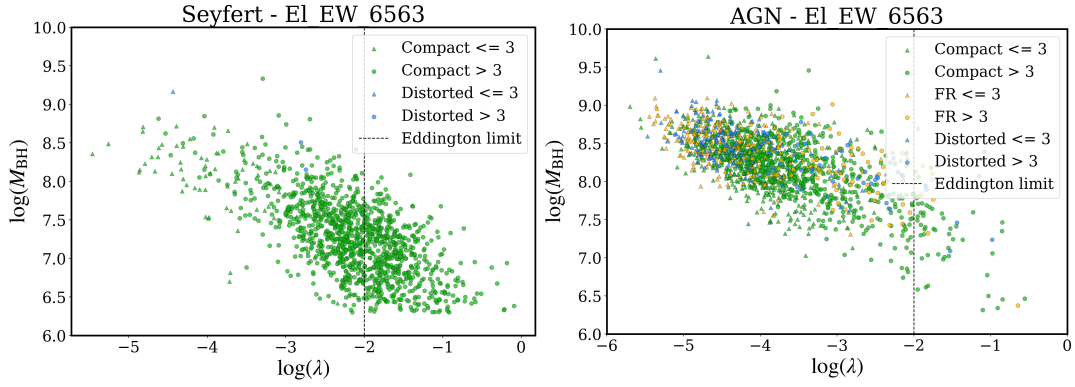


Figure 33: Black hole mass (M_{BH}) vs. Eddington ratio (λ) of Seyfert galaxies and AGN. Bolometric luminosity (L_{bol}) used for the λ was calculated from the [OIII] line.

Same was found for the 1D KS test applied only on the black hole mass, to support the claims of different distributions between compact and extended galaxies. Sources with $\text{EW} > 3 \text{ \AA}$ have $p\text{-value} = 0.001$ and $D = 0.200$, while sources with $\text{EW} \leq 3 \text{ \AA}$ have $p\text{-value} = 1.23 \cdot 10^{-19}$ and $D = 0.293$, which is supporting that the compact and extended sources have two different distributions of black hole mass.

If we look at the distribution of total luminosity at 1.4 GHz ($L_{1.4, \text{total}}$) (Figure 34), as the function of Eddington ratio (λ) we can see that compact sources cluster between $\log(L_{1.4, \text{total}}) = 20$ and $\log(L_{1.4, \text{total}}) = 24$ for both AGN and Seyfert. Extended sources have higher values of total luminosities, clearly separating themselves on the plot.

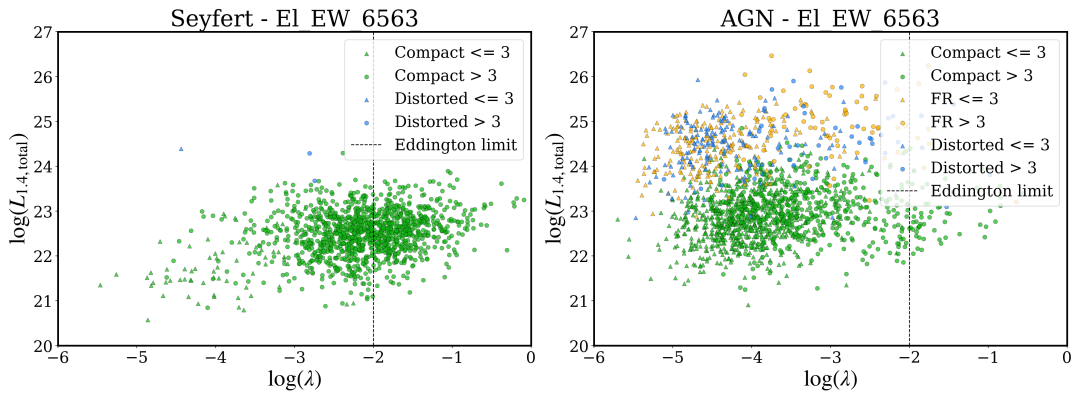


Figure 34: Total radio luminosity at 1.4 GHz ($L_{1.4, \text{total}}$) vs. Eddington ratio (λ) of Seyfert galaxies and AGN. Bolometric luminosity (L_{bol}) used for the λ was calculated from the [OIII] line.

8.4 Green Valley diagram

As discussed in [subsection 4.9](#), the reason why some radio galaxies do not reach large sizes might be due to their episodic radio activity. In fact, one mechanism which can reproduce this behaviour is due to the tidal distribution event, which allows matter to be accreted and thus form jets in a short period of time, as the matter comes in small packages. If this were the case, jet formation cannot be sustained for a longer period to form extended outflows ([Sullivan et al., 2024](#)). It was shown that the galaxies hosting the TDE are preferably located along the Green Valley region ([Yao et al., 2023](#)). In this section, we seek to find if similar behaviour in our sample of compact galaxies is seen, and thus see whether the jets in these sources could be due to the TDE.

To plot the green valley diagram, we first calculated the absolute magnitude for each filter of each object using the equation:

$$m - M = 5 \log(d) - 5, \quad (22)$$

where m is apparent magnitude, M is the absolute magnitude and d is distance to the source in parsecs.

After that, we estimated the absolute magnitudes corrected for extinction using the `EBVPY` repository ⁵, which calculates the $E(B - V)$ reddening value from dust maps from [Schlegel et al. \(1998\)](#). The extinction coefficients utilized for SDSS bands are $R_u = 4.15$, $R_g = 3.63$, $R_r = 3.22$, $R_i = 2.09$ and $R_z = 1.50$.

Next, we applied the k -correction as it was not included in the `ROGUE` catalogue. K -correction is used on galaxies that are further away from us as due to the cosmological redshift the wavelengths we observe are not the same as those emitted. We used the k -correction repository ⁶ (version 5.1.3) from [Blanton and Roweis \(2007\)](#). The colour $u - r$ was then calculated using the extinction-corrected as well as k -corrected absolute magnitudes. The green valley diagrams are plotted in [Figure 35](#).

As we can see in [Figure 35](#), Seyfert galaxies create a blue cloud below the green valley, as expected. However, Seyfert galaxies are a bit concentrated towards the Green Valley region of the plot, which is consistent with properties found among galaxies hosting TDEs. The galaxies classified as AGN reside higher on the diagram, creating the red sequence, with an older stellar population. However, their distribution also partially overlaps the green valley region of the plot.

We also created the green valley diagram with colour mapping by the total radio luminosity ($L_{1.4, \text{total}}$), shown in the [Figure 36](#). We found that galaxies with higher radio luminosity, which are predominantly extended sources, are located higher on the plot, mostly in the red sequence. Galaxies with lower luminosities are mainly in the blue cloud.

⁵EBVPY REPOSITORY: <https://github.com/rjsmethurst/ebvpy?tab=readme-ov-file>

⁶K-CORRECTION REPOSITORY: <https://kcorrect.readthedocs.io/en/5.1.3/intro.html>

The 2D KS test was applied on compact vs. extended AGN sources to find if the distribution is the same or not. p -value is $1.11 \cdot 10^{-33}$ and D is 0.302, suggesting two different distributions. We see that compact sources are indeed a bit shifted towards the smaller stellar masses with significant spread, while extended sources cluster around $\log(M_*) = 11.5$ (also seen in [Figure 25](#)), with almost no difference in the $u - r$ colour spread between the two samples.

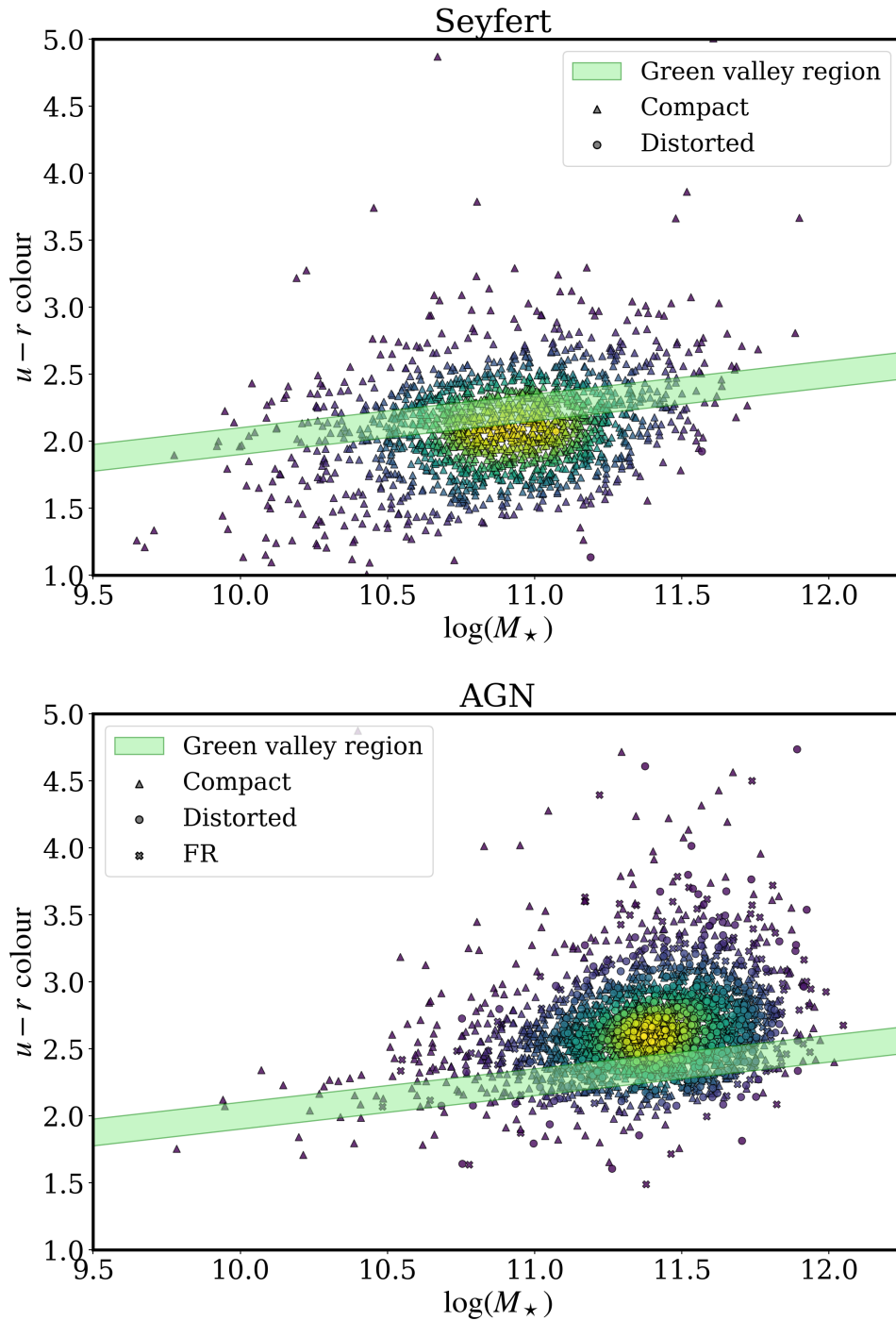


Figure 35: Seyfert galaxies and AGN plotted on a green valley diagram, with different shapes signifying compact, distorted and FR sources. The colour map represents the density of the plot.

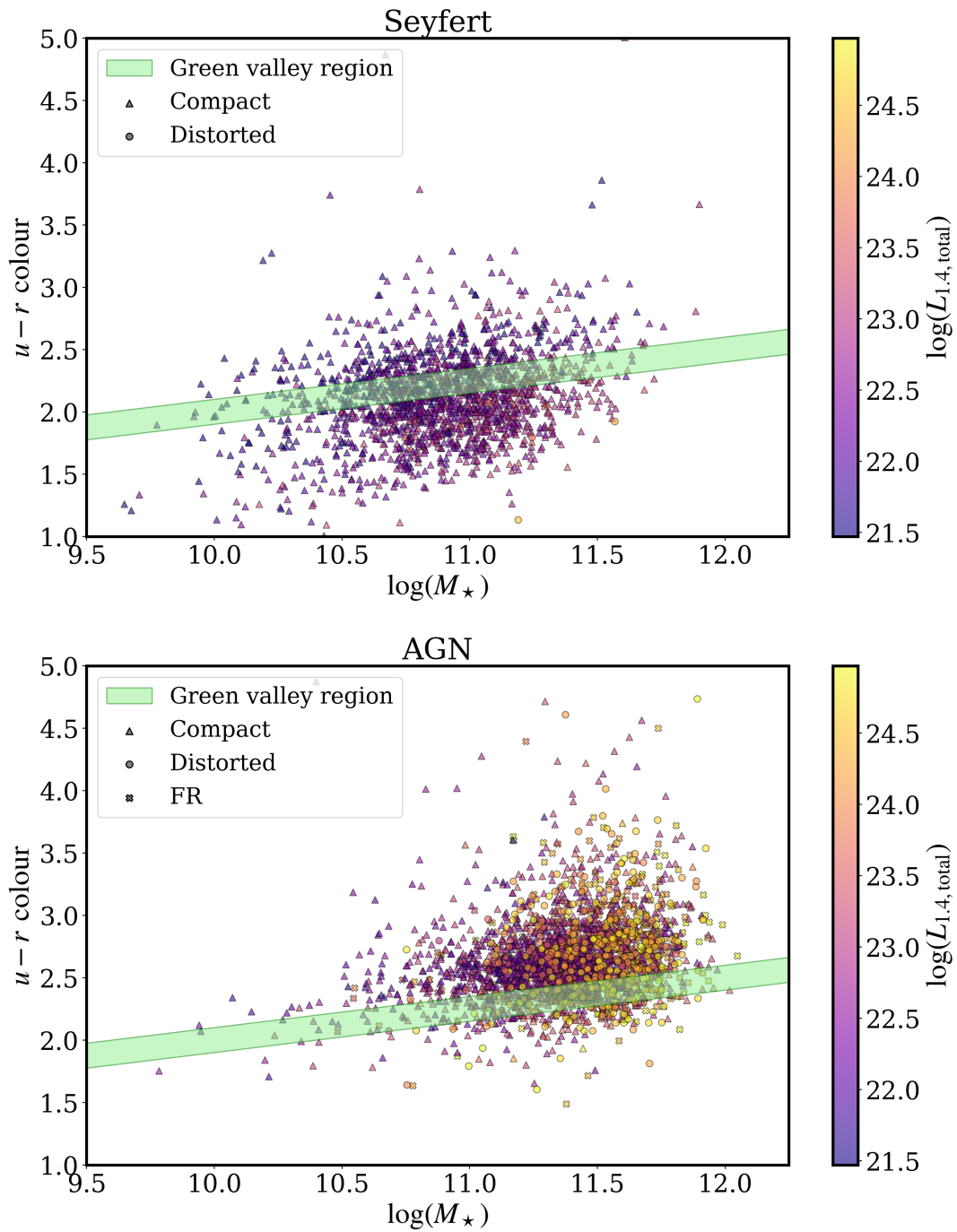


Figure 36: Seyfert galaxies and AGN galaxies plotted on a green valley diagram, with different shapes signifying compact, distorted and FR sources and colour maps indicating the total luminosity at 1,4 GHz ($L_{1.4, \text{total}}$).

9 Summary

In this thesis, we aim to find an answer as to why some radio galaxies form extended sources and others do not. To do so, we used the ROGUE (Optical Galaxies and having Unresolved or Extended morphologies) catalogue with results from the STARLIGHT code as supplementary material. In the case of Far Infrared and total radio luminosity at 1.4 GHz we also utilised the PSC and FSC datasets from the IRAS mission.

Firstly, to robustly identify AGN sources, we created the BPT diagram and removed those that had a line ratio consistent with star-forming galaxies. We then plotted the DLM diagram to investigate whether radio emission is dominated by AGN or SF regions. We found that some optical AGN are not classified as radio AGN according to the DLM diagram but rather fall into the SF category (we refer to them as Seyfert galaxies). The galaxies classified as FR I and FR II are mostly concentrated in the upper right corner, while galaxies classified as star-forming via the BPT diagram are in the lower left corner of the DLM plot.

Study of the relation of Far Infrared (FIR) and total radio luminosity at 1.4 GHz showed that sources with optical AGN classified via the BPT diagram, but with DLM classification as star-forming, can deviate from expected ratios obtained for typical star-forming regions. [Figure 17](#) and [Figure 18](#) show that most of these sources have a q factor around the value established for SF galaxies, still some galaxies show a radio excess, deviating by more than 1σ from this ratio. We attempted to correct the total radio emission from the contribution of star-forming regions. We utilised the [Murphy et al. \(2011\)](#) relation and SFR estimated by the STARLIGHT code and found that the radio emission is dominated by the AGN emission rather than the expected star-forming regions, which is not consistent with their FIR to 1.4 GHz ratio. This is likely a result of the underestimation of SFR by STARLIGHT, particularly in the dust-rich galaxies. Thus, we conclude that if we tried to correct the total radio luminosity by subtracting the contribution from the SF regions, we would only obtain the upper limit of the radio luminosity coming from the AGN.

We divided our sample into AGN and Seyfert galaxies and further studied them in more detail. First, we plotted the linear sizes as a function of the total radio luminosity at 1.4 GHz. Compact sources are unresolved by FIRST, so we adopted the FIRST beam size of 5.4 arcsec as the upper limit on their angular diameter. Both FR and distorted galaxies have typically larger linear sizes and much higher total luminosities than compact sources.

The redshift distribution showed that AGN tend to concentrate in the higher redshift, while compact Seyfert galaxies seem to peak at a smaller redshift. This is because AGN are predominantly elliptical galaxies, with higher luminosities and thus are easier to detect than Seyfert hosts as we increase the redshift.

Analysis of the optical morphology showed that Seyfert galaxies do not include any FR-like morphologies and have only three distorted radio morphologies. They are also hosted typically by galaxies with distorted, spiral, lenticular and elliptical morphologies in this order. The optical classification of AGN is less diverse. Elliptical galaxies represent around 97% of both distorted and FR radio galaxies, with negligible contribution of spiral or lenticular galaxies. Compact sources, on the other hand, are hosted in 91.2% by ellipticals, but the contribution of both distorted and lenticular galaxies cannot be neglected.

The stellar mass (M_*) showed that compact radio galaxies have typically smaller M_* than their extended counterparts, which is especially evident for compact Seyfert galaxies. The significance of this difference was confirmed with the KS test.

Studying the $A_{V,\text{Balmer}}$ revealed that there might have been some problem in the measurements or fitting procedures since the values, especially for AGN, are negative. Still, the compact sources show slightly higher dust presence along the line of sight. Compact Seyfert galaxies show the highest values of them all. The study of the A_V parameter showed similar propositions, and once again, we confirm the significance of the difference with the KS test.

We also found that while SFR shows that the AGN with compact radio morphologies might have smaller values than extended radio sources, the sSFR revealed that there is no significant difference between the subclasses of AGN, which was also proven by the KS test. Still, compact radio galaxies among Seyfert galaxies show the highest values, consistent with their classification as SF.

The BPT diagram for compact, extended, and FR-like radio AGN sources revealed no preferred clustering in the groups, also reinforced by the KS test.

The calculation of bolometric luminosity was done by two methods. Utilising the $H\alpha$ and [OIII] emission lines. By comparing the calculated luminosities to modelled ones obtained by [Stasińska et al. \(2025\)](#), we found that the [OIII] line gives us better approximations of the underlying bolometric luminosity. The Eddington ratio indicates that the Seyfert compact galaxies have an accretion disk in the transition from Shakura-Sunyaev to ADAF regime, while AGN are mostly consistent with the ADAF solution. There is also a difference between compact and extended AGN sources in terms of their Eddington ratio distributions. For compact AGN, sources with $EW > 3 \text{ \AA}$ peak around an Eddington ratio of -4.2 , while those with $EW \leq 3 \text{ \AA}$ peak closer to -3.6 , though with a broader distribution. Extended AGN with $EW > 3 \text{ \AA}$ show a peak near -5 , whereas those with $EW \leq 3 \text{ \AA}$ exhibit a wide spread with no clear peak.

The black hole masses (M_{BH}) obtained for radio AGN are typically higher than in Seyfert galaxies. Radio sources with compact morphology in AGN class have M_{BH} ranging between $\log(M_{\text{BH}}) = 6 - 9.5$ with Eddington ratio between $\log(\lambda) = -5$ and 0 , while extended sources usually are characterized

usually lower Eddington ratios and higher black hole masses. And generally, sources with extended radio morphology tend to have significantly higher luminosities than compact ones.

The last section talks about the possibility of compact sources being remnants of tidal disruption events. While there is no significant proof that the compact sources in the AGN sample reside mostly in the Green Valley region, a large fraction of compact sources from the Seyfert sample are identified in the Green Valley region. Thus, more in-depth focus studies are needed to better understand the source of radio emission in these sources.

To summarise, extended radio AGN are generally associated with larger linear sizes, higher stellar masses, higher fraction of elliptical hosts, lower extinction ($A_V, A_{V,\text{Balmer}}$), and higher 1.4 GHz luminosities. In contrast, compact AGN are more commonly found in distorted, spiral, or lenticular galaxies, with higher Eddington ratios, a broader range of black hole masses, and lower absolute but comparable specific star formation rates.

Bibliography

- [1] `scipy.stats.ks_2samp`, 2025. URL https://docs.scipy.org/doc/scipy/reference/generated/scipy.stats.ks_2samp.html#ks-2samp. Accessed: 2025-03-03.
- [2] R. D. Baldi. The nature of compact radio sources: the case of FR 0 radio galaxies. , 31(1):3, Dec. 2023. doi: 10.1007/s00159-023-00148-3.
- [3] J. A. Baldwin, M. M. Phillips, and R. Terlevich. Classification parameters for the emission-line spectra of extragalactic objects. , 93:5–19, Feb. 1981. doi: 10.1086/130766.
- [4] P. N. Best, G. Kauffmann, T. M. Heckman, et al. The host galaxies of radio-loud active galactic nuclei: mass dependences, gas cooling and active galactic nuclei feedback. , 362(1):25–40, Sept. 2005. doi: 10.1111/j.1365-2966.2005.09192.x.
- [5] M. R. Blanton and S. Roweis. K-Corrections and Filter Transformations in the Ultraviolet, Optical, and Near-Infrared. , 133(2):734–754, Feb. 2007. doi: 10.1086/510127.
- [6] R. J. Bouwens et al. Ultraviolet Luminosity Functions from 132 $z \sim 7$ and $z \sim 8$ Lyman-break Galaxies in the Ultra-deep HUDF09 and Wide-area Early Release Science WFC3/IR Observations. , 737(2):90, Aug. 2011. doi: 10.1088/0004-637X/737/2/90.
- [7] G. Bruzual and S. Charlot. Stellar population synthesis at the resolution of 2003. , 344(4):1000–1028, Oct. 2003. doi: 10.1046/j.1365-8711.2003.06897.x.
- [8] J. A. Cardelli, G. C. Clayton, and J. S. Mathis. The Relationship between Infrared, Optical, and Ultraviolet Extinction. , 345:245, Oct. 1989. doi: 10.1086/167900.
- [9] R. Cid Fernandes, G. Stasińska, Mateus, et al. A comprehensive classification of galaxies in the Sloan Digital Sky Survey: how to tell true from fake AGN? , 413(3):1687–1699, May 2011. doi: 10.1111/j.1365-2966.2011.18244.x.

- [10] N. E. Database. Fanaroff-riley classification, 2025. URL https://ned.ipac.caltech.edu/level5/Glossary/Essay_fanaroff.html. Accessed: 2025-03-05.
- [11] A. Del Moro et al. GOODS-Herschel: radio-excess signature of hidden AGN activity in distant star-forming galaxies. , 549:A59, Jan. 2013. doi: 10.1051/0004-6361/201219880.
- [12] A. Ermash. The Luminosity function of Narrow-Line Seyfert galaxies based on SDSS DR7 data. *arXiv e-prints*, art. arXiv:1304.7144, Apr. 2013. doi: 10.48550/arXiv.1304.7144.
- [13] B. L. Fanaroff and J. M. Riley. The morphology of extragalactic radio sources of high and low luminosity. , 167:31P–36P, May 1974. doi: 10.1093/mnras/167.1.31P.
- [14] L. Ferrarese and D. Merritt. A Fundamental Relation between Supermassive Black Holes and Their Host Galaxies. , 539(1):L9–L12, Aug. 2000. doi: 10.1086/312838.
- [15] K. Gebhardt, R. Bender, Bower, et al. A Relationship between Nuclear Black Hole Mass and Galaxy Velocity Dispersion. , 539(1):L13–L16, Aug. 2000. doi: 10.1086/312840.
- [16] T. M. Heckman and P. N. Best. The Coevolution of Galaxies and Supermassive Black Holes: Insights from Surveys of the Contemporary Universe. , 52:589–660, Aug. 2014. doi: 10.1146/annurev-astro-081913-035722.
- [17] G. Helou, B. T. Soifer, and M. Rowan-Robinson. Thermal infrared and nonthermal radio : remarkable correlation in disks of galaxies. , 298: L7–L11, Nov. 1985. doi: 10.1086/184556.
- [18] G. Helou, I. R. Khan, Malek, et al. IRAS Observations of Galaxies in the Virgo Cluster Area. , 68:151, Oct. 1988. doi: 10.1086/191285.
- [19] E. P. Hubble. A spiral nebula as a stellar system, Messier 31. , 69:103–158, Mar. 1929. doi: 10.1086/143167.
- [20] E. P. Hubble. *Realm of the Nebulae*. 1936.
- [21] G. Kauffmann et al. The host galaxies of active galactic nuclei. , 346(4): 1055–1077, Dec. 2003. doi: 10.1111/j.1365-2966.2003.07154.x.
- [22] L. J. Kewley, M. A. Dopita, Sutherland, et al. Theoretical Modeling of Starburst Galaxies. , 556(1):121–140, July 2001. doi: 10.1086/321545.

- [23] J. Kormendy and L. C. Ho. Coevolution (Or Not) of Supermassive Black Holes and Host Galaxies. , 51(1):511–653, Aug. 2013. doi: 10.1146/annurev-astro-082708-101811.
- [24] D. Koziel-Wierzbowska, A. Goyal, and N. Żywucka. Radio Sources Associated with Optical Galaxies and Having Unresolved or Extended Morphologies (ROGUE). I. A Catalog of SDSS Galaxies with FIRST Core Identifications. , 247(2):53, Apr. 2020. doi: 10.3847/1538-4365/ab63d3.
- [25] D. Koziel-Wierzbowska, N. V. Asari, Stasińska, et al. Identifying radio-active galactic nuclei among radio-emitting galaxies. *The Astrophysical Journal*, 910(1):64, mar 2021. doi: 10.3847/1538-4357/abe308. URL <https://dx.doi.org/10.3847/1538-4357/abe308>.
- [26] M. S. Longair. *Galaxy Formation*. Springer, Berlin, Germany, 2008. ISBN 978-3-540-73477-2.
- [27] F. J. Massey. The kolmogorov-smirnov test for goodness of fit. *Journal of the American Statistical Association*, 46(253):68–78, 1951. ISSN 01621459, 1537274X. URL <http://www.jstor.org/stable/2280095>.
- [28] Meyer-Hofmeister, E. and Meyer, F. Broad iron emission lines in seyfert galaxies – re-condensation of gas onto an inner disk below the adaf? *AA*, 527:A127, 2011. doi: 10.1051/0004-6361/201015478. URL <https://doi.org/10.1051/0004-6361/201015478>.
- [29] E. J. Murphy et al. Calibrating Extinction-free Star Formation Rate Diagnostics with 33 GHz Free-free Emission in NGC 6946. , 737(2):67, Aug. 2011. doi: 10.1088/0004-637X/737/2/67.
- [30] R. Narayan and I. Yi. Advection-dominated Accretion: Underfed Black Holes and Neutron Stars. , 452:710, Oct. 1995. doi: 10.1086/176343.
- [31] NASA, 2024. URL <https://science.nasa.gov/universe/galaxies/types/#lenticular-galaxies>. Accessed: 2025-01-31.
- [32] NASA Fermi Science Team. Active galactic nuclei, 2025. URL <https://fermi.gsfc.nasa.gov/science/eteu/agn/>. Accessed: 2025-02-27.
- [33] NASA Goddard Space Flight Center. Infrared astronomical satellite, 2024. URL <https://lambda.gsfc.nasa.gov/product/iras/index.html>. Accessed: 2024-02-28.
- [34] NASA HEASARC. Iras psc, 2024. URL <https://heasarc.gsfc.nasa.gov/W3Browse/iras/iraspsc.html>. Accessed: 2024-02-28.
- [35] NASA/IPAC Infrared Science Archive. Iras fsc, 2024. URL <https://irsa.ipac.caltech.edu/IRASdocs/surveys/fsc.html>. Accessed: 2024-02-28.

- [36] NRAO/AUI/NSF. Vla. Image, 2025. URL <https://public.nrao.edu/gallery/outstanding-in-wide-field/>. Accessed: 2025-03-03.
- [37] C. P. O’Dea and D. J. Saikia. Compact steep-spectrum and peaked-spectrum radio sources. *MNRAS*, 29(1):3, Dec. 2021. doi: 10.1007/s00159-021-00131-w.
- [38] T. J. Pearson, R. A. Perley, and A. C. S. Readhead. Compact radio sources in the 3C catalog. *MNRAS*, 90:738–755, May 1985. doi: 10.1086/113782.
- [39] RAL Space. IRAS – 40 years on, 2024. URL <https://www.ralspace.stfc.ac.uk/Pages/IRAS-40-years.aspx>. Accessed on [2025-03-03].
- [40] S. Rosswog and M. Brüggen. *Introduction to High-Energy Astrophysics*. Cambridge University Press, Cambridge, UK, 2007. ISBN 978-0521674423.
- [41] S. Salim. Green Valley Galaxies. *Serbian Astronomical Journal*, 189:1–14, Dec. 2014. doi: 10.2298/SAJ1489001S.
- [42] D. J. Schlegel, D. P. Finkbeiner, and M. Davis. Maps of Dust Infrared Emission for Use in Estimation of Reddening and Cosmic Microwave Background Radiation Foregrounds. *ApJ*, 500(2):525–553, June 1998. doi: 10.1086/305772.
- [43] N. I. Shakura and R. A. Sunyaev. Black holes in binary systems. Observational appearance. *Sov. Astron. J.*, 24:337–355, Jan. 1973.
- [44] M. Sikora, G. Stasińska, Kozieł-Wierzbowska, et al. Constraining Jet Production Scenarios by Studies of Narrow-line Radio Galaxies. *MNRAS*, 765(1): 62, Mar. 2013. doi: 10.1088/0004-637X/765/1/62.
- [45] G. Stasińska, R. Cid Fernandes, Mateus, et al. Semi-empirical analysis of Sloan Digital Sky Survey galaxies - III. How to distinguish AGN hosts. *MNRAS*, 371(2):972–982, Sept. 2006. doi: 10.1111/j.1365-2966.2006.10732.x.
- [46] G. Stasińska, N. Vale Asari, A. Wójtowicz, and D. Kozieł-Wierzbowska. Optically active and optically inactive radio galaxies as sub-populations of the main galaxy sample of the SDSS. *MNRAS*, 693:A135, Jan. 2025. doi: 10.1051/0004-6361/202452022.
- [47] A. G. Sullivan, R. D. Blandford, Begelman, et al. Small-scale radio jets and tidal disruption events: a theory of high-luminosity compact symmetric objects. *Monthly Notices of the Royal Astronomical Society*, 528(4):6302–6311, 02 2024. ISSN 0035-8711. doi: 10.1093/mnras/stae322. URL <https://doi.org/10.1093/mnras/stae322>.
- [48] Syrte. ndtest, 2025. URL <https://github.com/syrte/ndtest>. Accessed: 2025-03-03.

- [49] J. Sánchez Almeida, B. G. Elmegreen, C. Muñoz-Tuñón, and D. M. Elmegreen. Star formation sustained by gas accretion. *The Astronomy and Astrophysics Review*, 22(1), July 2014. ISSN 1432-0754. doi: 10.1007/s00159-014-0071-1. URL <http://dx.doi.org/10.1007/s00159-014-0071-1>.
- [50] E. Tempel, E. Saar, L. J. Liivamägi, et al. Galaxy morphology, luminosity, and environment in the SDSS DR7. , 529:A53, May 2011. doi: 10.1051/0004-6361/201016196.
- [51] S. Tremaine, K. Gebhardt, Bender, et al. The Slope of the Black Hole Mass versus Velocity Dispersion Correlation. , 574(2):740–753, Aug. 2002. doi: 10.1086/341002.
- [52] R. C. E. van den Bosch. Unification of the fundamental plane and Super Massive Black Hole Masses. , 831(2):134, Nov. 2016. doi: 10.3847/0004-637X/831/2/134.
- [53] P. C. van der Kruit. Observations of core sources in Seyfert and normal galaxies with the Westerbork synthesis radio telescope at 1415 MHz. , 15:110–122, Nov. 1971.
- [54] van Velzen et al. Seventeen tidal disruption events from the first half of ztf survey observations: Entering a new era of population studies. *The Astrophysical Journal*, 908(1):4, Feb. 2021. ISSN 1538-4357. doi: 10.3847/1538-4357/abc258. URL <http://dx.doi.org/10.3847/1538-4357/abc258>.
- [55] E. L. Wright. A Cosmology Calculator for the World Wide Web. , 118 (850):1711–1715, Dec. 2006. doi: 10.1086/510102.
- [56] Y. Yao, V. Ravi, Gezari, et al. Tidal Disruption Event Demographics with the Zwicky Transient Facility: Volumetric Rates, Luminosity Function, and Implications for the Local Black Hole Mass Function. , 955(1):L6, Sept. 2023. doi: 10.3847/2041-8213/acf216.
- [57] F. Yuan and R. Narayan. Hot Accretion Flows Around Black Holes. , 52: 529–588, Aug. 2014. doi: 10.1146/annurev-astro-082812-141003.
- [58] M. S. Yun, N. A. Reddy, and J. J. Condon. Radio Properties of Infrared-selected Galaxies in the IRAS 2 Jy Sample. , 554(2):803–822, June 2001. doi: 10.1086/323145.